



HAL
open science

A brittle failure model for long-period seismic events recorded at Turrialba volcano, Costa Rica

Thomas S. Eyre, Christopher J. Bean, Louis De Barros, Francesca Martini, Ivan Lokmer, Mauricio M. Mora, Javier F. Pacheco, Gerardo J. Soto

► **To cite this version:**

Thomas S. Eyre, Christopher J. Bean, Louis De Barros, Francesca Martini, Ivan Lokmer, et al.. A brittle failure model for long-period seismic events recorded at Turrialba volcano, Costa Rica. *Journal of Geophysical Research*, 2015, pp.10.1002/2014JB011108. 10.1002/2014JB011108 . hal-01142480

HAL Id: hal-01142480

<https://hal.science/hal-01142480>

Submitted on 15 Apr 2015

HAL is a multi-disciplinary open access archive for the deposit and dissemination of scientific research documents, whether they are published or not. The documents may come from teaching and research institutions in France or abroad, or from public or private research centers.

L'archive ouverte pluridisciplinaire **HAL**, est destinée au dépôt et à la diffusion de documents scientifiques de niveau recherche, publiés ou non, émanant des établissements d'enseignement et de recherche français ou étrangers, des laboratoires publics ou privés.

1 **A brittle failure model for long-period seismic events recorded at Turrialba volcano, Costa**
2 **Rica**

3 Thomas S. Eyre ^{a, 1}, Christopher J. Bean ^a, Louis De Barros ^{a, 2}, Francesca Martini ^{a, 3}, Ivan
4 Lokmer ^a, Mauricio M. Mora ^{b, e}, Javier F. Pacheco ^c and Gerardo J. Soto ^d

5 ^a *Seismology and Computational Rock Physics Laboratory, School of Geological Sciences,*
6 *University College Dublin, Belfield, Dublin 4, Ireland. tomyre2@gmail.com,*
7 *Chris.Bean@ucd.ie, ivan.lokmer@ucd.ie*

8 ^b *Escuela Centroamericana de Geología, Universidad de Costa Rica, San José, Costa Rica.*
9 *mauricio.mora@ucr.ac.cr*

10 ^c *Ovsicori-UNA, Universidad Nacional, Heredia, Costa Rica. jpacheco@una.ac.cr*

11 ^d *Terra Cognita Consultores, San José, Costa Rica. katomirodriguez@yahoo.com*

12 ^e *Red Sismológica Nacional (RSN: UCR-ICE), San José, Costa Rica*

13 ¹ *Now at: Department of Physics, University of Alberta, Edmonton, AB, T6G 2G7, Canada.*
14 *teyre@ualberta.ca*

15 ² *Now at: Géoazur, Université de Nice Sophia-Antipolis, CNRS, Observatoire de la Côte d'Azur,*
16 *250 rue Albert Einstein, Sophia-Antipolis, 06560 Valbonne, France. debarros@geoazur.unice.fr*

17 ³ *Now at: Tullow Oil Ltd, Dublin, Ireland. Francesca.Martini@tullowoil.com*

18

19 **Corresponding Author:** Thomas S. Eyre, Department of Physics, University of Alberta,
20 Edmonton, AB, T6G 2G7, Canada. (teyre@ualberta.ca)

21

22 **Key Points**

23 Pulse-like LPs have been inverted for their source locations and mechanisms

24 Scaling laws in the data are also investigated

25 Observations of LPs at Turrialba corroborate a brittle failure source model

26

27 **Abstract**

28 A temporary seismic network, consisting of 23 broadband and 6 short period stations, was
29 installed in a dense network at Turrialba volcano, Costa Rica, between 8th March and 4th May
30 2011. During this time 513 long-period (LP) events were observed. Due to their pulse-like
31 waveforms, the hypothesis that the events are generated by a slow failure mechanism, based on a
32 recent new model by Bean et al. (2014), is tested. A significant number (107) of the LPs are
33 jointly inverted for their source locations and mechanisms, using full-waveform moment tensor
34 inversion. The locations are mostly shallow, with depths < 800 m below the active Southwest
35 Crater. The results of the decompositions of the obtained moment tensor solutions show
36 complex source mechanisms, comprised of high proportions of isotropic and low, but seemingly
37 significant, proportions of compensated linear vector dipole (CLVD) and double couple
38 components. It is demonstrated that this can be explained as mode I tensile fracturing with a
39 strong shear component. The source mechanism is further investigated by exploring scaling laws

40 within the data. The LPs recorded follow relationships very similar to those of conventional
41 earthquakes, exhibiting frequency-magnitude and corner frequency vs magnitude relationships
42 that can be explained by brittle failure. All of these observations indicate that a slow failure
43 source model can successfully describe the generation of short duration LP events at Turrialba
44 volcano.

45 ***Index Terms:*** *volcanology; seismology; natural hazards*

46 ***Keywords:*** *volcano; seismicity; long period (LP) events; source inversion; Turrialba volcano;*
47 *scaling laws*

48 **1. Introduction**

49 Turrialba volcano (3340 m.a.s.l.) is a stratovolcano located at the eastern edge of the Cordillera
50 Volcánica Central, Costa Rica, Central America, 35km ENE of the capital San José (figure 1a).
51 Activity at the volcano has increased in recent years, with intensifying fumarolic gas discharges,
52 especially in the active Southwest Crater; summit inflation detected from 2005 to 2007; increases
53 in seismicity; and recent minor phreatic explosions (Campion et al., 2012; Martini et al., 2010;
54 Soto and Mora, 2013; Tassi et al., 2004; Vaselli et al., 2010). Monitoring the volcano is
55 therefore extremely important, as its close proximity to San José means that a large eruption has
56 the potential to adversely affect 1.5 million people (Soto et al., 2010).

57 A previous study was carried out into the source processes of long period (LP) seismic events
58 recorded at Turrialba volcano in 2009 (Eyre et al., 2013), where LPs were inverted for their
59 mechanism using full-waveform moment tensor inversion. Similar to studies conducted at other
60 volcanoes, a crack source mechanism was obtained, in the case of Turrialba dipping shallowly
61 towards the southwest. For the 2009 dataset this was interpreted, drawing on the Chouet (1986)

62 model of LP sources, as resonance within cracks in the hydrothermal system that follow
63 weaknesses in the volcano edifice, or as hydrothermal fluids “pulsing” through the cracks.
64 However, the authors state that a deformation-based source process could not be ruled out, as
65 this was postulated as the cause of similar events observed on Mt Etna (De Barros et al., 2011).

66 A second experiment at Turrialba volcano was undertaken in 2011, building on the work carried
67 out through the 2009 experiment and benefiting from the experience gained. The new
68 experiment is one of the first to be designed specifically to obtain more accurate moment tensor
69 inversion results for LP events, by incorporating more broadband seismometers into the network,
70 especially in the summit region of the volcano. Enhanced coverage of the summit area has been
71 demonstrated in previous studies to improve the moment tensor solutions (Bean et al., 2008; De
72 Barros et al., 2011). As well as improved solutions, this is also a more in-depth study than that
73 of Eyre et al. (2013), with moment tensor inversion applied to over 100 events.

74 During the experiment, Turrialba volcano was undergoing large-scale degassing, with up to ~
75 3000 tonnes of SO₂ per day expelled into the atmosphere (Campion et al., 2012). The majority
76 of this gas was released from a large fumarole located high on the southwest inner wall of the
77 Southwest Crater, which opened during a minor phreatic eruption in January 2010. 20
78 broadband (five 60 s and three 30 s) and 6 short-period (1 s) seismometers were installed in a
79 temporary network between 8th March and 4th May 2011, in addition to a 3 station permanent
80 broadband network (stations VTCE, VTCG, VTUN). Figure 1b shows a map of the network.
81 The non-active craters (the Northeast Crater and part of the Central Crater) allow for a dense
82 deployment of stations in the summit region of the volcano. The network consisted of three
83 seismic arrays and 13 stand-alone stations. Seismic arrays were located at TOMA, PIGA and
84 BABO. TOMA consisted of the 6 short-period stations in the shape of a cross, with the long axis

85 pointing to the active Central and Southwest Craters and an inter-station spacing of
86 approximately 60 m. The arrays BABO and PIGA consisted of 5 stations each, in a “T” shape
87 with their long axes pointing to the summit region. All stations had a sampling rate of 100 Hz.
88 The station WCR1 was located on the rim of the active Southwest Crater, within 100 m of the
89 main fumarole, and WCR2 is also located on the crater rim. As the LPs in 2009 were located in
90 this region at shallow depths (Eyre et al., 2013), it is likely both stations were very close to the
91 source of the seismicity. However, the close proximity to the strong gas discharge caused these
92 stations to record strong continuous energy in the 5 Hz to 40 Hz range.

93 There are currently two main categories of source models available for LP events: (1) the
94 resonating crack/conduit model (Chouet, 1986; 1988; Neuberg et al., 2006), and (2) a very
95 recently proposed slow brittle rupture model (Bean et al., 2014). In the first model, the lack of
96 high frequency content of the events is explained by relating the source processes causing the
97 events to fluid processes. A fluid-filled cavity is excited into resonance, inducing slow
98 dispersive waves (crack waves) which propagate along the cavity interface, interfering
99 constructively to produce the LPs observed. By definition this process leads to resonating
100 seismograms. The second model attributes the low corner frequencies of the events to slow
101 failure of unconsolidated volcanic material at shallow depths on volcanoes caused by the low
102 internal friction angles of the material. Rupture simulations show that this process leads to
103 pulse-like seismograms when not contaminated by path effects.

104 Examples of LP events recorded in 2011 and their corresponding spectra can be seen in figure 2,
105 recorded on station WCR1, low pass filtered at 5 Hz to remove the strong noise due to degassing
106 above this frequency. The main energy of the events is generally from 0.3 to 1.3 Hz. The events
107 exhibit pulse-like waveforms and therefore the brittle failure model appears to be more likely to

108 fit the data, as there is no resonance in the waveform which would be expected according to the
109 cavity resonance model. As the LP waveforms on Turrialba volcano are non-resonating, by
110 analyzing the waveforms, source locations, source mechanisms and the scaling laws of these
111 events, this study aims to determine if the slow failure model can reasonably explain the LP
112 events observed on Turrialba volcano.

113 **2. LP Event Identification**

114 513 LP events were recorded between 8th March and 4th May 2011. These LPs are identified
115 using the STA/LTA algorithm described in Eyre et al. (2013) for station TCCR, where the
116 STA/LTA method is implemented for both a low frequency band (0.2 – 4.0 Hz) and a high
117 frequency band (6.0 – 10.0 Hz) and the events are only picked when the STA/LTA value in the
118 low frequency band is three times that of the high frequency band. An average of 9 events per
119 day are detected.

120 LPs are filtered in a frequency band of 0.3 - 1.3 Hz (the frequency band in which they have most
121 energy) and then correlated in an attempt to group them into families of similar events using a
122 closed cluster technique (Eyre et al., 2013; Saccorotti et al., 2007) for 10 s windows of the Z
123 component at summit station TCCR. No families of more than 5 events with a correlation
124 coefficient greater than 0.75 could be found, suggesting that these events are not produced by a
125 repetitive source. Hence the events are treated individually.

126 **3. Full-Waveform Moment Tensor Inversion**

127 **3.1 Method**

128 Following previous studies by Chouet et al. (2003), Kumagai et al. (2005), Kumagai et al.
129 (2010), Nakano and Kumagai (2005), Ohminato et al. (1998) and Eyre et al. (2013),

130 simultaneous full-waveform moment tensor inversions to calculate the source mechanisms and
 131 grid searches for source locations are performed. The method is implemented identically to Eyre
 132 et al. (2013), with the exception of the velocity model. In the frequency domain, the n th
 133 component of the displacement u , recorded at position \mathbf{x} and frequency ω , can be written as:

$$134 \quad u_n(\mathbf{x}, \omega) = G_{np,q}(\mathbf{x}, \omega) \cdot M_{pq}(\omega) + G_{np}(\mathbf{x}, \omega) \cdot F_p(\omega), \quad n, p, q \text{ in } \{x, y, z\} \quad (1)$$

135 where M_{pq} is the force couple in the direction pq , F_p is the single force acting in the direction p ,
 136 and G_{np} and $G_{np,q}$ are the n th components of the Green's functions and their spatial derivatives
 137 with respect to the source coordinates, respectively, generated by the single force F_p and the
 138 moment M_{pq} , respectively. Green's functions are the displacement responses recorded at the
 139 receivers when an impulse force function is applied at the source position in an elastic Earth (the
 140 medium response). The summation convention applies. Equation (1) is linear, and in the
 141 frequency domain can be written in matrix form:

$$142 \quad \mathbf{d} = \mathbf{Gm} \quad (2)$$

143 where \mathbf{d} is the data matrix, \mathbf{G} contains the Green's functions, and \mathbf{m} contains the moment tensor
 144 and single forces components. As the LP events are recorded in the near field, P- and S- waves
 145 are intertwined. The near field effect is accurately taken into account in our Green's functions
 146 calculations, allowing for a full waveform inversion. The quality of the inversion results is
 147 tested through the evaluation of the misfit between the calculated and the observed data, herein
 148 referred to as the residual R :

$$149 \quad R = \frac{(\mathbf{d} - \mathbf{Gm})^T \mathbf{W} (\mathbf{d} - \mathbf{Gm})}{\mathbf{d}^T \mathbf{W} \mathbf{d}} \quad (3)$$

150 where \mathbf{W} is a diagonal matrix of weights for the quality of the data (in this study the data quality
151 is good for all stations and components and therefore all of the weights are fixed to 1: the
152 inversion intrinsically preferentially weights stations closer to the source). The inversion is
153 carried out in the 0.3 - 1.3 Hz frequency band used for the correlations (section 2) for 12 s time
154 windows, utilizing all components at all available stations.

155 In order to locate the events, the inversion is implemented for a grid of 2536 possible source
156 points in a 4000 m by 4000 m by 2000 m volume below the summit region of the volcano
157 (Chouet et al., 2003; Kumagai et al., 2005; Kumagai et al., 2010; Nakano et al., 2003; Ohminato
158 et al., 1998), with a grid spacing of 80 m in the summit region and 200 m further from the
159 summit. The number of possible source positions is much greater than the number of stations
160 used in the inversion (15 stand-alone broadband stations are available for the inversion), so the
161 Reciprocity Theorem (Aki and Richards, 2002) is used when computing the Green's functions
162 between the sources and receivers. The most probable source location is defined by the grid
163 point with the smallest misfit between observed and reconstructed data.

164 The Green's functions are calculated using a 3D elastic lattice method to simulate full-wavefield
165 seismic wave propagation (O'Brien and Bean, 2004). The model includes topography which has
166 been shown to be important for an accurate inversion in volcanic environments (Ripperger et al.,
167 2003). The shallow velocity structure has also been shown to be important in inversions (Bean
168 et al., 2008). As no model is currently available for Turrialba volcano (Eyre et al., 2013), the
169 shallow velocity structure is investigated using surface wave dispersion analysis using the three
170 available arrays (see section 1). The technique used is the multichannel analysis of surface
171 waves (MASW) method (Wathelet et al., 2004). However, this analysis is very limited due to
172 the small aperture of the arrays (the maximum station spacing is 180 m due to the steep

173 topography of the volcano). Although the results are confined to the very near-surface, analysis
174 shows that a low velocity layer exists at Turrialba volcano as has been found on many other
175 volcanoes (Bean et al., 2008, and references therein). Hence the numerical model used for
176 simulating the Green's functions includes a low velocity layer of 1039 m/s (P-wave) and 600 m/s
177 (S-wave), tracking the topography. However, as the surface wave inversion is not well
178 constrained, and we do not want to include an unrealistic poorly constrained step in the model
179 which would act as an unrealistic waveguide, we choose the smoothest model that fits the results.
180 Therefore the velocities within the layer are gradated to 100 m depth, beneath which the model is
181 homogeneous with a P-wave velocity of 2300 m/s and an S-wave velocity of 1328 m/s. Density
182 is related via the equation $\rho = 1700 + 0.2v_p$, where v_p is the P-wave velocity (Gardner et al.,
183 1974; O'Brien and Bean, 2009).

184 As the inversion is performed in the frequency domain without any assumption on the source
185 time history, an inverse FFT of the solution \mathbf{m} from the inversion of equation 2 leads to a source
186 time function for every component of the moment tensor and single forces. In order to obtain a
187 common source-time function, the moment tensor solutions are decomposed into their principle
188 components, using the method of Vasco (1989). This method involves the singular value
189 decomposition of the obtained six time-dependent moment tensor components. A common
190 source-time function for all six moment tensor components and its contribution to each are
191 obtained, thus giving a source-time history of the source process and its mechanism. The
192 eigenvalues of the "static" moment tensor give the pressure and tension values along the
193 principal axes (eigenvectors) from which the source mechanism can be reconstructed. From this,
194 the solution can be decomposed into the percentage of isotropic, compensated linear vector
195 dipole (CLVD) and double couple source mechanisms (Vavryčuk, 2001). Hence, for example, a

196 tensile crack source (often calculated as the most likely mechanism for LPs at volcanoes (e.g.
197 Cusano et al., 2008; De Barros et al., 2011)) produces a $\lambda : \lambda : (\lambda + 2\mu)$ ratio of moment tensor
198 eigenvalues (where λ and μ are the Lamé parameters) (Aki and Richards, 2002), which is 1 : 1 : 3
199 for a Poisson's ratio of 0.25 and 1 : 1 : 2 for a Poisson's ratio of 0.33.

200 Inversions are carried out both excluding and including single forces in the solutions. Single
201 forces are physically realistic in volcanic environments (for example due to mass transfer, drag
202 forces or volcanic jets) (Chouet, 2003; Takei and Kumazawa, 1994). However De Barros et al.
203 (2011) and De Barros et al. (2013) state that errors in modeling the velocity structure mainly
204 contaminate the single forces, leading to spurious single forces, while the moment tensor
205 solution is still correct. In particular, De Barros et al. (2013) showed using radiation patterns that
206 strong spurious forces, of the order of those usually derived from the moment tensors of real
207 data, can be produced from the P-to-S conversions at the interfaces between two different
208 materials. Since these interfaces are usually unknown in the shallow part of volcano, single
209 forces cannot be taken into account when interpreting results. On the other hand, De Barros et al.
210 (2011) suggest that the single forces will accommodate most of the errors, so they should be
211 included in the inversion procedure but should not be interpreted as part of the source solution.
212 Including single forces in the solution appears to stabilize the results obtained using the 2011
213 data and therefore this paper focusses chiefly on results for which single forces are included in
214 the inversion procedure. The single forces themselves are not interpreted as even though they
215 can be physically realistic in volcanic environments, they appear contaminated by model errors.
216 Emphasis was also placed on the results which included single forces in the inversion procedure
217 for the 2009 experiment (Eyre et al., 2013).

218 Constrained moment tensor inversion is also performed to test the robustness of the solutions,
219 with the source mechanism constrained as (1) an isotropic source and (2) a crack with a grid
220 search for the optimum dip and azimuth (for details, see Lokmer et al. (2007), De Barros et al.
221 (2011)). We reiterate that the single forces terms can accommodate model errors (De Barros et
222 al., 2013) and are therefore not physically interpreted. The number of data for every inversion is
223 3 components \times 15 stations \times N_f (number of frequency points). The number of unknowns
224 decreases from $9 \times N_f$ for the moment tensor + single forces inversion to $6 \times N_f$ (moment tensor
225 only inversion) and $4 \times N_f$ for crack + single forces constrained inversion.

226 As moment tensor inversion takes into account the amplitudes recorded at each station, site
227 amplification effects between stations must be removed to gain accurate solutions. These are
228 measured using the RMS amplitudes of the coda waves of several teleseismic earthquakes that
229 were recorded during each experiment on all stations (e.g. Zecevic et al., 2013), filtered between
230 0.3 and 1.3 Hz. The earthquakes used were located between 1000 and 1500 km from Turrialba
231 volcano and had magnitudes greater than 5.5 so that the coda for each event contained a
232 measurable low frequency component.

233 As the LP events do not appear to group well into families, moment tensor inversion is carried
234 out for a significant proportion (107 events, $\sim 20\%$) of all of the LP events observed. The
235 events chosen are those with optimal signal-to-noise ratios (generally the larger events), in order
236 to give an accurate inversion solution. We expect that inverting a large sample of LPs observed
237 at Turrialba volcano will yield a representative picture of all LP seismicity at Turrialba volcano.

238 **3.2 LP Location Results**

239 Joint inversions and grid searches are implemented for 107 events, filtered between 0.3 and 1.3
240 Hz. An example of the results of the grid search location technique for a single event is shown in
241 figure 3. The figure shows three slices through the grid of possible source locations used for the
242 inversions, with each grid point colored according to the residual obtained in the moment tensor
243 inversion for that grid point. The vertical slices are taken through the minimum residual, while
244 the horizontal slice is located at a depth of 2660 m.a.s.l. (680 m below the summit). The most
245 likely locations (the points with the lowest residuals) are shown in blue. It can be seen that the
246 resolution in the horizontal plane is very good, with the location between the active Southwest
247 and Central Craters, while the depth is less well constrained, but is less than 800 m below the
248 summit.

249 Figure 4a shows the best locations for inversions including single forces for all 107 inverted
250 events, in map view and W-E and S-N cross-sections. Most of the events are clustered tightly
251 below the active Southwest and Central Craters above 2500 m.a.s.l., i.e. shallower than 800 m
252 depth below the summit. The scattering in the source area may be due to uncertainty in the
253 medium velocity, but as these events do not belong to a family it is not surprising that the
254 sources are scattered in a region. The results in the x - y plane are consistent with the results of
255 array analysis, and are also very similar to solutions obtained when single forces are not included
256 in the inversion (figure 4b), demonstrating the robustness of the solutions. However the
257 locations obtained when single forces are included in the inversion appear to cluster closer
258 together and there are a smaller number of outliers than for inversions excluding single forces,
259 suggesting greater reliability in the results.

260 **3.3 LP Source Mechanism Results**

261 Moment tensor inversion solutions for the source locations with the lowest residuals are
262 investigated by fixing the location and redoing the inversion. An example of the results from a
263 single LP event when single forces are included in the inversion is shown in figure 5. Note the
264 pulse-like waveforms of the obtained moment tensor solution. The normalized waveform fits
265 between the real and reconstructed data are also shown, showing good fits for the summit
266 stations but poorer fits at more distal stations due to the intrinsic weighting of the stations by
267 their recorded amplitudes. This is acceptable due to the strong oscillating path effects at stations
268 further from the source (Bean et al., 2014). An eigenvector diagram is also shown, constructed
269 using a method from Chouet et al. (2003) where the eigenvectors are calculated every 0.01 s
270 when the amplitude of one of the moment tensor components is greater than 90 % of the
271 maximum amplitude. Finally, as described in section 3.1, singular value decomposition (Vasco,
272 1989) is used to extract a common source-time function with the scalar moment tensor
273 containing its value for each component. The eigenvectors are oriented with the long
274 eigenvector 21° from vertical (this angle is herein named θ) and an azimuth anticlockwise from
275 east (herein named φ) of 332° , with eigenvalues of 1.0 : 1.2 : 1.8. From the moment tensor
276 decomposition of Vavryčuk (2001), this result is 74 % isotropic. However, there is one larger
277 eigenvalue and two shorter eigenvalues, suggesting that the mechanism can be described as a
278 crack. This is demonstrated in the decomposition where compensated linear vector dipole
279 (CLVD) components are found to contribute 18 % to the solution. If the source is a pure tensile
280 crack then the long eigenvector is orthogonal to the crack plane, hence θ gives the dip angle and
281 φ the dip direction. The results however also show a double couple component in both cases of 9
282 % . It is therefore difficult to visualize the source mechanism. We reiterate that the single forces

283 term tends to “absorb” model errors (De Barros et al., 2013) but the forces themselves are not
284 reliable, and are not constrained further.

285 In order to determine whether these complex results are unique to this one LP event, 107 events
286 are inverted and summarized in figure 6. The results of the moment tensor decomposition
287 (Vavryčuk, 2001) (6a and b), and the orientations of the largest eigenvectors (θ and φ) (6c) are
288 shown. Primarily the figure shows results for inversions where single forces are included, but
289 figure 6a also shows results for moment tensor only solutions for comparison and completeness.
290 The results of the principal component analysis are shown as histograms in figure 6a. The
291 comparison between the results of inversions including and omitting single forces shows that
292 similar distributions of results are resolved for each (i.e. similar peaks in the histograms), but the
293 standard deviations in component percentages for inversions including single forces are much
294 smaller. It is more likely that source mechanisms for LP events observed at the same volcano do
295 not vary to a large degree, and therefore these findings corroborate the work of De Barros et al.
296 (2013) who (as previously stated) suggest that moment tensor solutions from inversions
297 including single forces are more reliable. This supports our decision to focus on results obtained
298 when single forces are included in the inversions. Figure 6b shows the results including single
299 forces as a triangular graph to show the full range of results. The triangular graph also shows the
300 residual from the moment tensor inversion for each event using a color scale. A strong isotropic
301 component is evident for all events, peaking at $\sim 75\%$. The CLVD and double couple
302 components are much less significant but do appear to contribute, with the CLVD component
303 peaking at $\sim 5\%$ but for some events contributing up to 40% , and the double couple peaking at
304 $\sim 10\%$ but for some events up to 45% . The variability here, together with the different source-

305 time functions, is consistent with the LP events not presenting as families, i.e. events look
306 different as the source mechanisms are different.

307 The mechanism orientations are shown in figure 6c, both for the unconstrained inversions (MT +
308 F) and for inversions when the source is constrained as a crack mechanism with a grid search on
309 the orientation (Crack + F). The color scale refers to the residuals obtained for the moment
310 tensor inversion. The solutions obtained with the unconstrained inversions are compatible and
311 validated with the crack constrained inversions, however the crack constrained inversions do not
312 reproduce all the complexities associated with the unconstrained inversions. Although there is a
313 large scatter in the results, it can be seen that for the majority of the events (especially when the
314 residual is small) that θ is relatively small (30° or less). The cracks are therefore shallowly
315 dipping, meaning that φ can be quite unstable. There also appears to be a preferential φ
316 direction, with most events orientated with a φ of approximately 180° to 200° anticlockwise from
317 east, i.e. due west, and perhaps a smaller cluster orientated roughly in the opposite direction
318 (340° - 360° , due east). Therefore the cracks change dip around the horizontal position, from
319 slightly eastward to the slightly westward dipping. Again, the variability in the orientations is
320 consistent with the lack of similarity between event waveforms.

321 **3.4 Joint Inversion and Grid Search Results: Discussion**

322 The LPs are located at shallow depths below the volcano (< 800 m). The results for the events
323 with the lowest residuals, suggesting the most reliable inversions, mostly give depths between
324 700 and 800 m below the summit, although this may be several hundred meters shallower or
325 deeper due to the uncertainty in the velocity model which can strongly affect the depth
326 determination. However, the shallow results are in good agreement with LPs previously

327 observed at Turrialba volcano (Eyre et al., 2013) and with results at other volcanoes, including
328 Kilauea, Hawaii (Almendros et al., 2001), Campi Flegrei, Italy (Cusano et al., 2008), Mt Etna,
329 Sicily (De Barros et al., 2009; De Barros et al., 2011; Lokmer et al., 2007; Saccorotti et al.,
330 2007), Piton de la Fournaise, La Réunion (Zecevic et al., 2013), and Kusatsu-Shirane, Japan
331 (Kumagai et al., 2002; Nakano et al., 2003).

332 Most of the events appear to be closely clustered together below the active Southwest Crater.
333 This is again in good agreement with results from 2009 (Eyre et al., 2013). There are several
334 events that appear to be outliers, however. It is most likely that these outliers are erroneous, as
335 they generally have higher residuals and are poorly constrained. The shallow locations below
336 the active crater suggest a relationship with shallow processes and this needs to be taken into
337 account when interpreting the mechanisms.

338 The moment tensor inversion results suggest that the source mechanisms are strongly isotropic.
339 However, the mechanisms also appear to have small CLVD and double couple components. As
340 stated in section 3.1, the single force components are likely to be unreliable and are not
341 interpreted physically. These results suggest a very complex source mechanism. An isotropic
342 and CLVD mechanism combined is interpreted as a crack mechanism. With a small contribution
343 from double couple included, the mechanisms could be interpreted as a crack mechanism with a
344 small amount of shearing, akin to a transtensional or transpressional crack mechanism. A
345 method for determining the mechanism parameters for this type of source is described in
346 Vavryčuk (2001). A tensile earthquake (an earthquake with tensile faulting or combining shear
347 faulting and tensile faulting) can be described using a slip vector that is not restricted to orient

348 within the fault plane and deviates from the fault plane, causing its opening or closing. This slip
349 vector is labelled $[\vec{u}]$, and has an angle from the fault plane (labelled Σ) of α (figure 7a).

350 α and the λ/μ ratio (κ) at the source can be calculated using:

$$351 \quad \kappa = \frac{4}{3} \left(\frac{c^{\text{ISO}}}{c^{\text{CLVD}}} - \frac{1}{2} \right) \quad (4)$$

$$352 \quad \alpha = \sin^{-1} \left(3 \frac{M_{\text{max}}^* + M_{\text{min}}^*}{|M_{\text{max}}^*| + |M_{\text{min}}^*|} \right) \quad (5)$$

353 (Vavryčuk, 2001), where M_{max}^* and M_{min}^* are defined as the maximum and minimum deviatoric
354 eigenvalues of the moment tensor solution, and c^{ISO} and c^{CLVD} correspond to the components of
355 isotropic and CLVD energy, respectively. The angle between the normal to the fault and the
356 tension (\vec{T}) axis is $\beta = 45^\circ - \alpha/2$, and this is also the angle between the slip vector and the tension
357 axis. The angle (θ) between the tension axis and vertical is calculated using the eigenvectors of
358 the moment tensor solution. From this, the orientation of the fault plane from vertical (δ) can be
359 calculated using $\delta = \theta - \beta$.

360 The results are investigated for events with residuals obtained from the moment tensor inversion
361 of less than 0.25 to remove events for which the mechanisms are more poorly resolved. Events
362 with source locations that appear to be outliers are also removed. For the remaining 42 events
363 the average of the double-couple components is 16 %, of the isotropic components is 72 % and
364 of the CLVD components is 12 %. The standard deviations are 8 %, 8 % and 9 %, respectively.
365 The relationship between α and the proportion of double-couple, isotropic and CLVD
366 components can be plotted, as shown here in figure 7b (Vavryčuk, 2001) for the mean value of κ
367 of 7.3. Low values of α correspond to a high degree of shearing as the slip vector is almost

368 parallel to the fault plane whereas high values of α correspond to tensile mechanisms. Using
369 solutions with residuals lower than 0.25, the mean of the absolute values of α is 21° , while β is
370 34° , θ is 23° , and δ is -12° . The schematic geometry of the slip movement is shown in figure 7a,
371 with the relationships between α and the percentage of isotropic, double couple and CLVD
372 components (figure 7b). This shows that, even with a large value for the isotropic component, a
373 small value of α can be found, i.e. the source mechanism does not deviate much from a shearing
374 movement. Intuitively the results are very surprising as an α of 21° suggests a strong shear
375 component and a low tensile component, apparently at odds with the small double couple
376 component calculated from the decompositions of the solutions. Figure 7c shows a histogram of
377 the distribution of α for all events inverted. There appears to be a large variability in α from -60°
378 to 60° , and the standard deviation of α is 27° . Negative values of α suggest transpressional
379 fracturing and positive values suggest transtensional fracturing, however due to potential errors
380 from mismodeling the velocity structure we do not believe that it is possible to accurately resolve
381 the polarity of α . The low angles calculated for α therefore strongly support the possibility of a
382 combined tensile-shear mechanism. Double couple components have been observed in other
383 studies of LP events (Cusano et al., 2008). However, as the principal models of LP source
384 mechanisms attribute them to fluid oscillation processes, these components are often interpreted
385 as insignificant, or explained as errors resulting from the calculation of the Green's functions. In
386 such cases, it is possible to interpret the source mechanism as a crack, as was construed in the
387 2009 study of Eyre et al. (2013). However as the double couple component is similar in size to
388 the CLVD component it would be difficult to justify including the CLVD component in the
389 interpretation while ignoring the double couple.

390 If the LP source is truly a tensile-shear mechanism, unidirectional slip motion should be
391 observed in the source-time function, i.e. the band-limited response to a ramp function. To
392 investigate whether this is the case, the source-time function obtained from singular value
393 decomposition of the moment tensor solution for an LP event is shown plotted in figure 8a, along
394 with the band-limited signal (band-pass filtered between 0.5 and 1.3 Hz) produced by the ramp
395 function shown in figure 8b which has a rise time of 0.5 s. As expected, the onset and overall
396 shape of both signals are similar; however the LP source-time function shows some extra higher
397 frequency fluctuations later in the signal. These could be caused by errors in the inversions such
398 as mismodeling of the velocity structure, leading to some path effects mapping into the source-
399 time function. Nevertheless as the mechanism has a tensile component the source-time function
400 is likely to be more complicated than in the case of simple shear. The opening of a crack is
401 followed by a closing, as the pressure within strongly decreases during opening (Eaton et al.
402 2014). This means that tensile mechanisms only exhibit a small unidirectional movement. In the
403 case of LP events at Turrialba volcano, as the source is complex, involving both the opening and
404 closing plus shearing of the crack, the source-time function is also more complex than for the
405 simple shearing case, which may explain the source-time function observed. The source-time
406 function that we reconstruct is therefore fully compatible with a tensile-shear mechanism.

407 The obtained κ values should provide an indication of the fractured material. The mean κ value
408 of 7.3 corresponds to a Poisson's ratio of ~ 0.44 . Such high values suggest that the source region
409 either consists of (1) highly fractured or porous media saturated with fluids (as P-wave velocities
410 are driven by the fluids, while S-wave velocities depend on the solid frame), or (2) ductile media
411 (which may or may not be caused by high temperatures). For example, dense sands (which have
412 a ductile response to stress and are likely highly similar to the unconsolidated material typically

413 found at the near-surface in the summit regions of volcanoes) have a Poisson's ratio of 0.45
414 (Greaves et al., 2011). As fluids, structural heterogeneities, unconsolidated materials and high
415 temperatures are likely to be present in the shallow part of the volcano, either of these are strong
416 possibilities. However, it must also be taken into account that the obtained value of κ can be
417 strongly influenced by the accuracy of the velocity model.

418 **4. Scaling Laws of LP Events**

419 The results outlined above show that the events are caused by a tensile mechanism with a likely
420 strong shear component. These results can be well explained by the new source model for LP
421 events of Bean et al. (2014) where the events are generated by slow failure in the shallow edifice.
422 However, further analysis of the LP events is necessary to investigate how well the model
423 corroborates the data and to explore brittle failure as a valid model. Tectonic earthquake
424 seismology uses empirical scaling laws to link the seismological observations to the source
425 properties, and the above observations encourage us to apply such analysis to these LP data to
426 further investigate their source.

427 **4.1 Frequency-magnitude relation**

428 The frequency-magnitude relation (Gutenberg and Richter, 1944; Ishimoto and Iida, 1939)
429 usually gives a b -value of approximately $b = 1$ for tectonic earthquakes. Figure 9 shows a plot of
430 the LP event maximum amplitudes (plotted logarithmically to use as a proxy for magnitude)
431 against the cumulative number of events for the LPs observed at Turrialba volcano during the
432 2011 experiment, recorded on station TCCR (which has a higher signal-to-noise ratio than
433 WCR1). Amplitude can be used as a proxy for magnitude only for earthquakes which are at the
434 same distance from the station, which is satisfied here. It is noted that the slope of cumulative

435 number versus amplitude in log-log plot is actually known as the m -value (Ishimoto and Iida,
436 1939). Above the visually estimated detection threshold of $\sim 3 \times 10^{-6}$ m/s the relationship
437 appears to show non power-law scaling with a deficit of larger events.

438 One possible interpretation for this behavior is that the steepest gradient (-2.9, line shown in
439 figure 9) corresponds to the true b -value and the real detection threshold is $\sim 2 \times 10^{-5}$ m/s. Note
440 that here we assume that amplitude is proportional to the magnitude ($b = m$), but even if we
441 assume a relationship of $m = b + 1$ instead (Suzuki, 1959), we obtain $b = 1.9$ which is still higher
442 than that observed for ordinary earthquakes. The smaller events (amplitude $< 2 \times 10^{-5}$ m/s) do
443 not fit the relationship due to the variable levels of noise (e.g. volcanic tremor) resulting in an
444 incomplete catalogue. Other potential issues include the relatively small size of the catalogue
445 and the small magnitude range of the catalogue (~ 2 orders of magnitude). For amplitudes below
446 $\sim 3 \times 10^{-6}$ m/s, the graph is flat as the events are no longer detectable. In this interpretation larger
447 LPs occur less often than expected based on the typical earthquake scaling law. However, large
448 b -values have been observed for earthquakes and volcano-tectonic (VT) events in volcanic areas,
449 e.g. at Mt. St. Helens and Mt. Spurr (Wiemer and McNutt, 1997), Mt. Pinatubo (Sánchez et al.,
450 2004) and the off-Ito volcanic region (Wyss et al., 1997), so this is also feasible for LPs. Warren
451 and Latham (1970) state that b -values up to 3 are possible in earthquakes induced by high
452 thermal gradients, supported by Wiemer and McNutt (1997). Another possibility is that the high
453 b -value could be caused by high heterogeneity of the material where the fracturing occurs (Mogi,
454 1962) and/or a low stress regime (Schorlemmer et al., 2005), both of which are highly likely at
455 shallow depths on volcanoes. Finally, Wiemer and McNutt (1997) also propose that increased
456 pore pressure due to heating of the groundwater could increase pore pressure and so lower
457 effective stress, which is also very likely at shallow depths beneath the Southwest Crater at

458 Turrialba volcano. The high b -value of the LPs could therefore be caused by a combination of
459 these factors.

460 Nonetheless, it is felt that the section of the graph with a lower gradient occurs over a much
461 larger range of amplitudes than would be expected if it was caused by incompleteness of the
462 catalogue. Therefore the behavior is interpreted as a real manifestation caused by the source
463 processes of the events. Bean et al. (2014) observed a similar non power-law scaling for failure
464 at the brittle-to-ductile transition in materials similar to those observed at the near-surface of
465 volcanoes simulated using a damage mechanics model. They also stated that this relationship is
466 very similar to magnitude-frequency relationships of LPs observed at Mt. Etna, Sicily and at
467 Turrialba volcano during the 2009 experiment. The observations made here are consistent with
468 these earlier findings.

469 **4.2 Corner frequency analysis**

470 Earthquakes follow a corner frequency (f_c) versus magnitude (M_0) scaling. The most commonly
471 used relationship is $M_0 \propto f_c^{-3}$ (Aki, 1967; Geller, 1976; Hiramatsu et al., 2002; Kanamori and
472 Rivera, 2004). Before this analysis is performed, we must first confirm that the LP spectra
473 appear similar to earthquake spectra, with flat spectra up to a corner frequency where the energy
474 begins to fall off (the fall off is often modeled using an ω^{-2} model). The unfiltered displacement
475 spectrum for the event from figure 2a is plotted in log-log scale in figure 10. This shows that the
476 events do behave like typical earthquakes, and a corner frequency can be picked. As previously
477 mentioned, the peak above 10 Hz corresponds to continuous noise (spectral estimates for pre-LP
478 signal noise are plotted in blue).

479 **4.2.1 Synthetic Tests**

480 A concern with implementing corner frequency analysis on LP events at volcanoes is that the
481 LPs are recorded in the near field and have a tensile component, since the corner frequency
482 concept is valid in the far field approximation for double couple mechanisms. On a theoretical
483 basis, Eaton et al. (2014) show that the corner frequency relationship is still valid for events with
484 tensile components. To investigate whether the corner frequencies can be accurately recovered
485 in the near field, synthetic tests are conducted.

486 The Stokes solution of elastic wave radiation (Aki and Richards, 2002; Lokmer and Bean, 2010)
487 is used to kinematically calculate synthetic seismograms. The near field and intermediate field
488 effects can be included in the calculations. In order to simulate finite fault ruptures, the source
489 comprises a 2D grid of “tensile crack” point sources representing the rupture plane. These point
490 sources rupture unilaterally along the longer dimension of the rupture plane. In order to yield a
491 range of event magnitudes the rupture plane ranges in size from 50 m to 1000 m long (with the
492 width equal to half of the length).

493 To test whether the relationship should hold specifically for the LP events recorded at Turrialba
494 volcano with the stations used, the rupture plane is located in a similar location to the recorded
495 LP events (UTM 196920 m E, 1108760 m N and 2660 m.a.s.l.), and has a similar orientation
496 with $\theta = 20^\circ$ and $\varphi = 190^\circ$. The first station tested is WCR1, which has the highest amplitudes
497 and least propagation effects for the events as it is closest to the source, and therefore would be
498 the optimum station to employ for source property studies.

499 In order to find the corner frequencies, the spectra of the synthetic events are fitted to the ω^{-2}
500 model using the equation:

501
$$A = \frac{1}{\sqrt{1 + \left(\frac{f}{f_c}\right)^4}} \quad (6)$$

502 where f is the frequency and f_c is the corner frequency (e.g. Abercrombie, 1995). The fit is
503 implemented for a range of corner frequencies to find the corner frequency with the optimum
504 least-squares fit between the equation and the data. The fit also outputs the amplitude for the flat
505 part of the spectrum of the event, which is used as a proxy for the magnitude.

506 The relationship between corner frequencies and magnitudes for the synthetic events in the far
507 field is shown in figure 11a, along with the fits between the spectra and fitting function. A
508 strong inverse relationship between the two is demonstrated as expected. The relationship is not
509 quite f_c^{-3} as is expected (the slope of the best fit line is -3.45 instead of -3). When the near field
510 (and intermediate field) term is included, invalidating the far-field assumption, the results are
511 worse, but an inverse relationship can still be recognized with a slope of -5.03 (figure 11b). To
512 check that this is a real problem caused by the close proximity to the source, the analysis is also
513 carried out at a station further from the source, station DIVI. Here the analysis results in
514 gradients of -3.13 and -2.57 excluding and including the near field term, respectively, much
515 closer to the expected solution of -3.

516 **4.2.2 Analysis of LP Data**

517 The synthetic analysis has shown that ideally a far field station should be used for the analysis in
518 order to reduce the near field effect. Unfortunately this is not possible as these stations have
519 much larger propagation effects included in the LP spectra (Bean et al., 2008) which can strongly
520 affect the results of seismic source studies (Giampiccolo et al., 2007), have a lower signal-to-
521 noise ratio and have a smaller range of LP event amplitudes. Therefore station WCR1, on the

522 rim of the active Southwest Crater, is used for the analysis. The synthetic tests have
523 demonstrated that the gradient of the best fit of the data cannot be interpreted but if an inverse
524 relationship is uncovered this still has implications for the source mechanism.

525 As the LPs recorded are relatively small (of the order of 1×10^{-5} m) in comparison to the
526 earthquakes usually analyzed using this method and the noise is quite high (as shown in figure
527 10), it is very difficult to determine the corner frequencies of the events. In order to overcome
528 this issue, the following procedure is implemented. The events are first extracted and cut into 10
529 s long traces before integrating into displacement. Their means and trends are removed, the
530 traces are tapered using a Hann window and are then transformed into the frequency domain.
531 The spectra are smoothed using a moving average. Corner frequencies of the events can now be
532 obtained using the same technique used for the synthetic data. Fits are implemented for a
533 frequency range of 0.3 to 7.0 Hz, just above the microseismic noise range.

534 The results of the analysis are shown in figure 12a. Figure 12b shows examples of the fit of the
535 ω^{-2} model used to calculate the corner frequencies with the data spectra of random individual
536 events. It can be seen that there does appear to be a relationship between the corner frequency
537 and the magnitude of the events. The L1 norm best fit has a gradient of -2.0 rather than the -3.0
538 expected in the dry, brittle fracture of earthquakes when analyzed in the far field. However, as
539 the noise and the distribution of the event sizes can bias the linear regression, we computed two
540 L1 norm linear regressions: the corner frequency as a function of the amplitude and the inverse
541 relationship. The average value we obtain for the gradient is -2.9, which is very close to the -3.0
542 expected. Therefore the f_c^{-3} relationship is consistent with the data. The observed inverse
543 relationship is consistent with a brittle failure origin for the Turrialba volcano LP events.

544 **5. Discussion**

545 The observations and results presented in this paper corroborate the possibility that LP events at
546 Turrialba volcano may be generated by a failure mechanism. First, LPs observed close to the
547 source (i.e. at the summit stations) are often pulse-like, and this is evidence that especially
548 conflicts with the Chouet (1986) model of fluid-filled cavity resonance. This fact could be
549 explained by a high damping of the resonance due to a high viscosity fluid or low crack wall
550 stiffness (Chouet, 1986), but it seems suspicious that a model to describe resonance should apply
551 for pulse-like waveforms. On the other hand, a material failure model does not require such
552 specific tuning.

553 Second, the frequency-magnitude relationship and corner frequency-magnitude relationships are
554 very similar to those observed in rock fracture experiments and earthquake studies. More work
555 is required to analyze whether other possible source mechanisms or triggers can cause the
556 relationships observed, but this goes beyond the scope of this paper. Together though, these
557 observations appear to suggest that a mechanical failure mechanism is more likely than a
558 resonant mechanism for LP event generation at Turrialba volcano.

559 Finally, the results from the moment tensor inversion suggest a tensile mechanism with a strong
560 shear component. This is difficult to explain using the Chouet (1986) model but can readily be
561 explained using the model of Bean et al. (2014) as tensile (mode I) cracks combined with
562 shearing, which results in transtensional- or transpressional-like faulting. Transtensional faults
563 seem especially plausible in volcanic environments due to flank instabilities and hydrofracture in
564 hydrothermal systems, and transpressional faults could be caused by gravitational collapse.
565 Dipping slump faults have been mapped at volcanoes, for example Stromboli (Apuani et al.,

566 2005), and shallow-dipping detachment faults have been proposed at Mt. Etna (Rust et al., 2005).
567 In the case of Stromboli, a VLP event was constrained as a slow-slip double couple event caused
568 by dip-slip (Cesca et al., 2007). This type of faulting fits well with the orientations of the
569 mechanisms obtained for the LPs at Turrialba volcano, as they have shallow dip angles.
570 Turrialba volcano sits within a SW-NE trending graben structure with a strike-slip component of
571 motion (Soto, 1988), however linking the tectonic regime to the LP mechanisms is very difficult
572 in the shallow part of the volcano as the stress regime can be completely altered by the presence
573 of fluids, topography effects, gravitational instability and structural heterogeneities near the
574 summit.

575 A likely underlying cause of the events observed at Turrialba volcano therefore appears to be
576 deformation. The majority of the events are located below the active Southwest and Central
577 Craters, as was also constrained for events recorded in 2009 (Eyre et al., 2013). This suggests
578 that small-scale deformation is occurring below these active craters. However, the recovered
579 source-time function is not accurate enough to distinguish between inflation, which could be
580 caused by an influx/rising of magma or hydrothermal processes, and deflation, which could be
581 due to the loss of large quantities of gas and edifice collapse. As previously mentioned, large
582 scale deformation has not been observed at Turrialba volcano since 2007 (Martini et al., 2010) so
583 the deformation causing LP events is likely to be small and localized beneath the active craters.
584 Future work is necessary to explore the slow failure model for LP event generation as described
585 by Bean et al. (2014), however the observations and analysis described in this paper suggest that
586 brittle failure is a possible LP generating mechanism on Turrialba volcano.

587 **Acknowledgements**

588 This work has been funded by Science Foundation Ireland (SFI), Contract No.
589 09/RFP/GEO2242. We are grateful to Red Sismológica Nacional (RSN: UCR-ICE), the Instituto
590 Costarricense de Electricidad (ICE), and OVSICORI-UNA for supporting the logistical work and
591 fieldwork. In particular we thank Carlos Redondo, Francisco *Chico* Arias, Geoffroy Avaré,
592 Megan Zecevic and Luciano Zucarello for their help during the fieldwork. We are also grateful
593 to the Cordillera Volcánica Central Conservation Area staff for the facilities provided during the
594 fieldwork at Turrialba Volcano National Park. Data to support this article are from a
595 collaborative project between UCD, RSN: UCR-ICE, ICE and OVSICORI-UNA. Because the
596 data has only been analyzed by one of these groups so far it cannot yet be released. Finally we
597 wish to thank Naofumi Aso, an anonymous reviewer, and the Associate Editor for their
598 comments which greatly improved the manuscript.

599

600 **References**

- 601 Abercrombie, R.E., 1995. Earthquake source scaling relationships from -1 to 5 ML using
602 seismograms recorded at 2.5-km depth. *Journal of Geophysical Research: Solid Earth*,
603 100(B12): 24015-24036, doi: 10.1029/95jb02397.
- 604 Aki, K., 1967. Scaling law of seismic spectrum. *Journal of Geophysical Research*, 72(4): 1217-
605 1231, doi: 10.1029/JZ072i004p01217.
- 606 Aki, K. and Richards, P.G., 2002. *Quantitative seismology* 2nd ed. University Science Books,
607 Sausalito, California, 700 pp.

608 Almendros, J., Chouet, B. and Dawson, P., 2001. Spatial extent of a hydrothermal system at
609 Kilauea Volcano, Hawaii, determined from array analyses of shallow long-period
610 seismicity 2. Results. *Journal of Geophysical Research*, 106(B7): 13581-13597, doi:
611 10.1029/2001jb000309.

612 Apuani, T., Corazzato, C., Cancelli, A. and Tibaldi, A., 2005. Stability of a collapsing volcano
613 (Stromboli, Italy): Limit equilibrium analysis and numerical modelling. *Journal of*
614 *Volcanology and Geothermal Research*, 144(1–4): 191-210, doi:
615 <http://dx.doi.org/10.1016/j.jvolgeores.2004.11.028>.

616 Bean, C.J., Lokmer, I. and O'Brien, G.S., 2008. Influence of near-surface volcanic structure on
617 long-period seismic signals and on moment tensor inversions: Simulated examples from
618 Mount Etna. *Journal of Geophysical Research*, 113(B8), doi: 10.1029/2007jb005468.

619 Bean, C.J., De Barros, L., Lokmer, I., Métaixian, J.P., O'Brien, G.S. and Murphy, S., 2014. Long-
620 period seismicity in the shallow volcanic edifice formed from slow-rupture earthquakes.
621 *Nature Geoscience*, 7: 71-75, doi: 10.1038/ngeo2027.

622 Campion, R., Martinez-Cruz, M., Lecocq, T., Caudron, C., Pacheco, J., Pinardi, G., Hermans, C.,
623 Carn, S. and Bernard, A., 2012. Space- and ground-based measurements of sulphur
624 dioxide emissions from Turrialba Volcano (Costa Rica). *Bulletin of Volcanology*: 1-14,
625 doi: 10.1007/s00445-012-0631-z.

626 Cesca, S., Braun, T., Tessmer, E. and Dahm, T., 2007. Modelling of the April 5, 2003, Stromboli
627 (Italy) paroxysmal eruption from the inversion of broadband seismic data. *Earth and*

628 Planetary Science Letters, 261(1–2): 164-178, doi:
629 <http://dx.doi.org/10.1016/j.epsl.2007.06.030>.

630 Chouet, B., 1986. Dynamics of a fluid-driven crack in three dimensions by the finite difference
631 method. Journal of Geophysical Research, 91(B14): 13967-13992, doi:
632 10.1029/JB091iB14p13967.

633 Chouet, B., 1988. Resonance of a fluid-driven crack: radiation properties and implications for the
634 source of long-period events and harmonic tremor. Journal of Geophysical Research,
635 93(B5): 4375-4400, doi: 10.1029/JB093iB05p04375.

636 Chouet, B., 2003. Volcano seismology. Pure and Applied Geophysics, 160(3): 739-788, doi:
637 10.1007/PL00012556

638 Chouet, B., Dawson, P., Ohminato, T., Martini, M., Saccorotti, G., Giudicepietro, F., De Luca,
639 G., Milana, G. and Scarpa, R., 2003. Source mechanisms of explosions at Stromboli
640 Volcano, Italy, determined from moment-tensor inversions of very-long-period data.
641 Journal of Geophysical Research, 108(B1), doi: 10.1029/2002jb001919.

642 Cusano, P., Petrosino, S. and Saccorotti, G., 2008. Hydrothermal origin for sustained Long -
643 Period (LP) activity at Campi Flegrei Volcanic Complex, Italy. Journal of Volcanology
644 and Geothermal Research, 177(4): 1035-1044, doi: 10.1016/j.jvolgeores.2008.07.019.

645 De Barros, L., Bean, C.J., Lokmer, I., Saccorotti, G., Zuccarello, L., O'Brien, G.S., Métaxian, J.-
646 P. and Patanè, D., 2009. Source geometry from exceptionally high resolution long period
647 event observations at Mt Etna during the 2008 eruption. Geophysical Research Letters,
648 36(24), doi: 10.1029/2009g1041273.

649 De Barros, L., Lokmer, I., Bean, C.J., O'Brien, G.S., Saccorotti, G., Métaxian, J.P., Zuccarello,
650 L. and Patanè, D., 2011. Source mechanism of long-period events recorded by a high-
651 density seismic network during the 2008 eruption on Mount Etna. *Journal of Geophysical*
652 *Research*, 116(B1), doi: 10.1029/2010jb007629.

653 De Barros, L., Lokmer, I. and Bean, C.J., 2013. Origin of spurious single forces in the source
654 mechanism of volcanic seismicity. *Journal of Volcanology and Geothermal Research*,
655 262(0): 1-6, doi: <http://dx.doi.org/10.1016/j.jvolgeores.2013.06.006>.

656 Eaton, D.W., van der Baan, M., Birkelo, B., and Tary, J-B, 2014. Scaling relations and spectral
657 characteristics of tensile microseisms: evidence for opening/closing cracks during
658 hydraulic fracturing. *Geophysical Journal International*, 196(3): 1844-1857, doi:
659 10.1093/gji/ggt498.

660 Eyre, T.S., Bean, C.J., De Barros, L., O'Brien, G.S., Martini, F., Lokmer, I., Mora, M.M.,
661 Pacheco, J.F. and Soto, G.J., 2013. Moment tensor inversion for the source location and
662 mechanism of long period (LP) seismic events from 2009 at Turrialba volcano, Costa
663 Rica. *Journal of Volcanology and Geothermal Research*, 258: 215-223, doi:
664 <http://dx.doi.org/10.1016/j.jvolgeores.2013.04.016>.

665 Gardner, G., Gardner, L. and Gregory, A., 1974. Formation velocity and density—the diagnostic
666 basics for stratigraphic traps. *Geophysics*, 39(6): 770-780, doi: 10.1190/1.1440465.

667 Geller, R.J., 1976. Scaling relations for earthquake source parameters and magnitudes. *Bulletin*
668 *of the Seismological Society of America*, 66(5): 1501-1523.

669 Giampiccolo, E., D'Amico, S., Patanè, D. and Gresta, S., 2007. Attenuation and source
670 parameters of shallow microearthquakes at Mt. Etna volcano, Italy. *Bulletin of the*
671 *Seismological Society of America*, 97(1B): 184-197, doi: 10.1785/0120050252.

672 Greaves, G.N., Greer, A.L., Lakes, R.S., and Rouxel, T., 2011. Poisson's ratio and modern
673 materials. *Nature Materials*, 10: 823-837, doi: 10.1038/nmat3134.

674 Gutenberg, B. and Richter, C.F., 1944. Frequency of earthquakes in California. *Bulletin of the*
675 *Seismological Society of America*, 34: 185-188.

676 Hiramatsu, Y., Yamanaka, H., Tadokoro, K., Nishigami, K., and Ohmi, S., 2002. Scaling law
677 between corner frequency and seismic moment of microearthquakes: Is the breakdown of
678 the cube law a nature of earthquakes? *Geophysical Research Letters*, 29(8): 1211, doi:
679 10.1029/2001g1013894.

680 Ishimoto, M. and Iida, K., 1939. Observations sur les seisms enregistre par le microseismograph
681 construit dernièrement. *Bulletin of the Earthquake Research Institute, University of Tokyo*
682 17: 443-478.

683 Kanamori, H. and Rivera, L., 2004. Static and dynamic scaling relations for earthquakes and
684 their implications for rupture speed and stress drop. *Bulletin of the Seismological Society*
685 *of America*, 94(1): 314-319, doi: 10.1785/0120030159.

686 Kumagai, H., Chouet, B. and Nakano, M., 2002. Waveform inversion of oscillatory signatures in
687 long-period events beneath volcanoes. *Journal of Geophysical Research*, 107(B11), doi:
688 10.1029/2001jb001704.

689 Kumagai, H., Chouet, B.A. and Dawson, P.B., 2005. Source process of a long-period event at
690 Kilauea volcano, Hawaii. *Geophysical Journal International*, 161(1): 243-254, doi:
691 10.1111/j.1365-246X.2005.02502.x.

692 Kumagai, H., Nakano, M., Maeda, T., Yepes, H., Palacios, P., Ruiz, M., Arrais, S., Vaca, M.,
693 Molina, I. and Yamashima, T., 2010. Broadband seismic monitoring of active volcanoes
694 using deterministic and stochastic approaches. *Journal of Geophysical Research*,
695 115(B8): B08303, doi: 10.1029/2009jb006889.

696 Lokmer, I., Bean, C.J., Saccorotti, G. and Patanè, D., 2007. Moment-tensor inversion of LP
697 events recorded on Etna in 2004 using constraints obtained from wave simulation tests.
698 *Geophysical Research Letters*, 34(22), doi: 10.1029/2007g1031902.

699 Lokmer, I. and Bean, C.J., 2010. Properties of the near-field term and its effect on polarization
700 analysis and source locations of long-period (LP) and very-long-period (VLP) seismic
701 events at volcanoes. *Journal of Volcanology and Geothermal Research*, 192(1-2): 35-47,
702 doi: 10.1016/j.jvolgeores.2010.02.008.

703 Martini, F., Tassi, F., Vaselli, O., Del Potro, R., Martinez, M., del Laat, R.V. and Fernandez, E.,
704 2010. Geophysical, geochemical and geodetical signals of reawakening at Turrialba
705 volcano (Costa Rica) after almost 150 years of quiescence. *Journal of Volcanology and*
706 *Geothermal Research*, 198(3-4): 416-432, doi: 10.1016/j.jvolgeores.2010.09.021.

707 Mogi, K., 1962. Magnitude-frequency relation for elastic shocks accompanying fractures of
708 various materials and some related problems in earthquakes. *Bulletin of the Earthquake*
709 *Research Institute, University of Tokyo*, 40: 831-853.

710 Nakano, M., Kumagai, H. and Chouet, B.A., 2003. Source mechanism of long-period events at
711 Kusatsu–Shirane Volcano, Japan, inferred from waveform inversion of the effective
712 excitation functions. *Journal of Volcanology and Geothermal Research*, 122(3-4): 149-
713 164, doi: 10.1016/s0377-0273(02)00499-7.

714 Nakano, M. and Kumagai, H., 2005. Response of a hydrothermal system to magmatic heat
715 inferred from temporal variations in the complex frequencies of long-period events at
716 Kusatsu-Shirane Volcano, Japan. *Journal of Volcanology and Geothermal Research*,
717 147(3-4): 233-244, doi: 10.1016/j.jvolgeores.2005.04.003.

718 Neuberg, J.W., Tuffen, H., Collier, L., Green, D., Powell, T. and Dingwell, D., 2006. The trigger
719 mechanism of low-frequency earthquakes on Montserrat. *Journal of Volcanology and*
720 *Geothermal Research*, 153(1-2): 37-50, doi: 10.1016/j.jvolgeores.2005.08.008.

721 O'Brien, G.S. and Bean, C., 2004. A 3D discrete numerical elastic lattice method for seismic
722 wave propagation in heterogeneous media with topography. *Geophysical Research*
723 *Letters*, 31(14), doi: 10.1029/2004GL020069.

724 O'Brien, G.S. and Bean, C.J., 2009. Volcano topography, structure and intrinsic attenuation:
725 Their relative influences on a simulated 3D visco-elastic wavefield. *Journal of*
726 *Volcanology and Geothermal Research*, 183(1-2): 122-136, doi:
727 10.1016/j.jvolgeores.2009.03.004.

728 Ohminato, T., Chouet, B.A., Dawson, P. and Kedar, S., 1998. Waveform inversion of very long
729 period impulsive signals associated with magmatic injection beneath Kilauea Volcano,

730 Hawaii. Journal of Geophysical Research, 103(B10): 23839-23862, doi:
731 10.1029/98jb01122.

732 Ripperger, J., Igel, H. and Wasserman, J., 2003. Seismic wave simulation in the presence of real
733 volcano topography. Journal of Volcanology and Geothermal Research, 128(1-3): 31-44,
734 doi: 10.1016/S0377-0273(03)00245-2.

735 Rust, D., Behncke, B., Neri, M. and Ciocanel, A., 2005. Nested zones of instability in the Mount
736 Etna volcanic edifice, Italy. Journal of Volcanology and Geothermal Research, 144(1-4):
737 137-153, doi: <http://dx.doi.org/10.1016/j.jvolgeores.2004.11.021>.

738 Saccorotti, G., Lokmer, I., Bean, C., Digrazia, G. and Patane, D., 2007. Analysis of sustained
739 long-period activity at Etna Volcano, Italy. Journal of Volcanology and Geothermal
740 Research, 160(3-4): 340-354, doi: 10.1016/j.jvolgeores.2006.10.008.

741 Sánchez, J.J., McNutt, S.R., Power, J.A. and Wyss, M., 2004. Spatial variations in the frequency-
742 magnitude distribution of earthquakes at Mount Pinatubo volcano. Bulletin of the
743 Seismological Society of America, 94(2): 430-438, doi: 10.1785/0120020244.

744 Schorlemmer, D., Wiemer, S. and Wyss, M., 2005. Variations in earthquake-size distribution
745 across different stress regimes. Nature, 437(7058): 539-542.

746 Soto, G.J., 1988. Estructuras volcano-tectónicas del volcan Turrialba, Costa Rica, America
747 Central, Actas Quinto Congreso Geológico Chileno, Santiago, pp. 163-175.

748 Soto, G.J., Mora, R., Mora, M.M., Barquero, R., Taylor, W., Vargas, A., Alvarado, G.E.,
749 Ramírez, C., González, G., Mora, R., Paniagua, C. and Fernández, J.F., 2010. Turrialba

750 volcano's threat to the cities of the Central Valley of Costa Rica, *Cities on Volcanoes* 6,
751 Puerto de la Cruz, Tenerife, pp. 138.

752 Soto, G.J. and Mora, M., 2013. Actividad del volcán Turrialba (2007-2011) y perspectivas de
753 amenaza volcánica, *Costa Rica en el tercer milenio: desafíos y propuestas para la*
754 *reducción de vulnerabilidad ante los desastres*, Preventec. UCR, pp. 287-310.

755 Suzuki, Z., 1959. A Statistical Study on the Occurrence of Small Earthquakes (IV). *Science*
756 *Reports of the Tohoku University, Ser. 5, Geophysics*, 11: 10-54.

757 Takei, Y. and Kumazawa, M., 1994. Why have the single force and torque been excluded from
758 seismic source models? *Geophysical Journal International*, 118(1): 20-30, doi:
759 10.1111/j.1365-246X.1994.tb04672.x

760 Tassi, F., Vaselli, O., Barboza, V., Fernandez, E. and Duarte, E., 2004. Fluid geochemistry and
761 seismic activity in the period 1998-2002 at Turrialba Volcano (Costa Rica). *Annals of*
762 *Geophysics*, 47(4): 1501-1511.

763 Vasco, D.W., 1989. Deriving source-time functions using principal component analysis. *Bulletin*
764 *of the Seismological Society of America*, 79(3): 711-730.

765 Vaselli, O., Tassi, F., Duarte, E., Fernandez, E., Poreda, R. and Huertas, A., 2010. Evolution of
766 fluid geochemistry at the Turrialba volcano (Costa Rica) from 1998 to 2008. *Bulletin of*
767 *Volcanology*, 72(4): 397-410, doi: 10.1007/s00445-009-0332-4.

768 Vavryčuk, V., 2001. Inversion for parameters of tensile earthquakes. *Journal of Geophysical*
769 *Research*, 106(B8): 16339-16355, doi: 10.1029/2001jb000372.

770 Warren, N.W. and Latham, G.V., 1970. An experimental study of thermally induced
771 microfracturing and its relation to volcanic seismicity. *Journal of Geophysical Research*,
772 75(23): 4455-4464, doi: 10.1029/JB075i023p04455.

773 Wathelet, M., Jongmans, D. and Ohrberger, M., 2004. Surface-wave inversion using a direct
774 search algorithm and its application to ambient vibration measurements. *Near Surface*
775 *Geophysics*, 2: 211-221.

776 Wiemer, S. and McNutt, S.R., 1997. Variations in the frequency-magnitude distribution with
777 depth in two volcanic areas: Mount St. Helens, Washington, and Mt. Spurr, Alaska.
778 *Geophysical Research Letters*, 24(2): 189-192, doi: 10.1029/96gl03779.

779 Wyss, M., Shimazaki, K. and Wiemer, S., 1997. Mapping active magma chambers by b values
780 beneath the off-Ito volcano, Japan. *Journal of Geophysical Research: Solid Earth*,
781 102(B9): 20413-20422, doi: 10.1029/97jb01074.

782 Zecevic, M., De Barros, L., Bean, C.J., O'Brien, G.S. and Brenguier, F., 2013. Investigating the
783 source characteristics of long-period (LP) seismic events recorded on Piton de la
784 Fournaise volcano, La Réunion. *Journal of Volcanology and Geothermal Research*, 258:
785 1-11, doi: <http://dx.doi.org/10.1016/j.jvolgeores.2013.04.009>.

786

787 **Figure Captions**

788 Figure 1 – (a) Map of the location of Turrialba volcano in Costa Rica. (b) Map of the 2011
789 broadband seismic network at Turrialba volcano, including an inset enlarged map of the summit
790 region. Solid triangles indicate stand-alone seismic stations and open triangles denote arrays of

791 stations. The approximate positions of the summit craters are outlined by red dashed lines,
792 labelled SW, C and NE to denote the Southwest, Central and Northeast Craters, respectively.
793 Contours are in m.a.s.l.

794

795 Figure 2 – (a) - (d) Examples of LP events recorded on the vertical component of summit station
796 WCR1 (shown filtered between 0.3 and 1.3 Hz in red as used in the moment tensor inversion)
797 and the corresponding frequency spectra. The events are low-pass filtered below 5 Hz to remove
798 the strong noise above this frequency believed to be caused by the strong degassing.

799

800 Figure 3 – Location of the LP event shown in figure 2a calculated using full waveform moment
801 tensor inversion for a 3D grid of possible source locations below the volcano. Low residuals
802 (blue) indicate likely locations. The vertical slices are through the point with the minimum
803 residual. The horizontal slice is located at 2660 m.a.s.l.. The result when single forces are not
804 included in the inversion is very similar. The optimum location is at shallow (< 800 m) depth
805 below the active Southwest (or edge of the Central) Crater.

806

807 Figure 4 – Location results for all 107 inverted LP events obtained using the moment tensor
808 inversion grid search method. Results for inversions including (a) and excluding (b) single
809 forces are shown. The colored markers show the location of the minimum residual for each
810 event, with the color and marker size corresponding to the number of events. The locations are
811 shown in map view (top panel) and west – east and north – south cross-sections (bottom left and

812 right respectively). The map view shows contours in m.a.s.l.. In both cases most of the events
813 are located below the active craters at shallow depths, however the results from inversions
814 including single forces are more tightly clustered, with fewer outliers.

815

816 Figure 5 – Results of the full waveform moment tensor inversion for the event shown in figure
817 2a for the source location with the lowest residual. The moment tensor solution (including single
818 forces) is shown top left, and the normalized waveform fits between the real (blue) and
819 reconstructed (red) data below (traces are 12 s long). The eigenvectors, sampled every 0.01 s, of
820 the moment tensor solution are also plotted (right).

821

822 Figure 6 – Collective results from the full waveform moment tensor inversion of all 107 LP
823 events. (a) The results of the principal component analysis from Vavryčuk (2001), with the
824 moment tensors decomposed into their proportions of isotropic, CLVD and double couple
825 components, for inversions excluding (MT) and including (MT + SF) single forces in the
826 solutions. The results are similar in both cases, but solutions including single forces show much
827 less spread, suggesting that they are less affected by errors in the inversion procedure. The
828 results are also illustrated for inversions including single forces in (b) in a triangle graph, to more
829 easily visualize the relationships for individual events. The residuals obtained for each inversion
830 are also shown according to the color scale. The results show a strong isotropic component for
831 most events, with lower but significant components of CLVD and double couple. (c) The
832 orientations of the principle eigenvectors for the unconstrained and crack constrained inversions
833 including single forces. Again the color scale indicates the residual obtained from the inversion.

834 θ is small for most events. For the events with low residuals, φ appears to be preferentially
835 orientated to $180^\circ - 200^\circ$ anticlockwise from east.

836

837 Figure 7 – (a) Average source mechanism for LP events with moment tensor solutions with
838 residuals lower than 0.25, plotted using the method of Vavryčuk (2001). The slip vector is
839 labelled $[\vec{u}]$, the fault plane is labelled Σ and \vec{T} is the tension axis. α is 21° , θ is 23° , and δ is -
840 12° . (b) Relationship between α and the double-couple (DC), isotropic (ISO) and CLVD
841 components for the source mechanisms of events with $\kappa = 7.3$ (corresponding to a Poisson's ratio
842 of ~ 0.44) at the source, using the relationship of Vavryčuk (2001). (c) Histogram of the number
843 of events with slip vector orientated for each 10° range of α .

844

845 Figure 8 – (a) Comparison between the source-time function obtained from singular value
846 decomposition of the moment tensor solution of an LP event from Turrialba volcano, filtered
847 between $0.5 - 1.3$ Hz (blue) and the signal obtained by filtering the ramp function with a rise
848 time of 0.5 s (b) in the same frequency band (red). Note the similarities between the two signals:
849 the first peak and overall shape. Higher frequency fluctuations observed later in the decomposed
850 signal may be caused by errors in the inversion procedure or may be due to the complex
851 interaction within the source of unidirectional shearing plus tensile opening and closing.

852

853 Figure 9 – LP event amplitudes (plotted in logarithmic scale as a proxy for magnitude) against
854 cumulative number of events greater than that amplitude. The catalogue appears to be complete

855 above the visually estimated detection threshold of $\sim 3 \times 10^{-6}$ m/s. The line of best fit for the
856 steepest section of the plot has a gradient of ~ -2.9 .

857

858 Figure 10 – Displacement frequency spectrum of the LP event from figure 2a recorded at WCR1,
859 in log-log scale (black). The noise spectrum taken before the event is also shown (blue),
860 demonstrating that the event spectrum is above the noise. The shape of the spectrum appears
861 similar to that of a regular earthquake, allowing a corner frequency to be picked. The peak
862 above 8 Hz corresponds to continuous noise and so is ignored in the corner frequency analysis.

863

864 Figure 11 – Relationship between corner frequency and magnitude for synthetically created
865 events located in a similar location to the real events and recorded at station WCR1. Also shown
866 are the fits between the synthetic event spectra and the function used to estimate the corner
867 frequencies. L denotes the length of the rupture plane. (a) shows the results for the far-field term
868 only, and (b) shows the results including the near-field term. The best fit lines are shown: (a) has
869 a slope of -3.45 and (b) has a slope of -5.03 . For ordinary earthquakes, -3 is expected. The
870 results suggest that the corner frequencies of events are affected by recording close to the source,
871 especially by the near-field term, however an inverse linear relationship is always present.

872

873 Figure 12 – Relationship between corner frequency and magnitude for LP events recorded at
874 Turrialba volcano for station WCR1. (a) shows the results from the corner frequency analysis of
875 the LP events. As the magnitude range is small and the fits are not exact, the events are quite

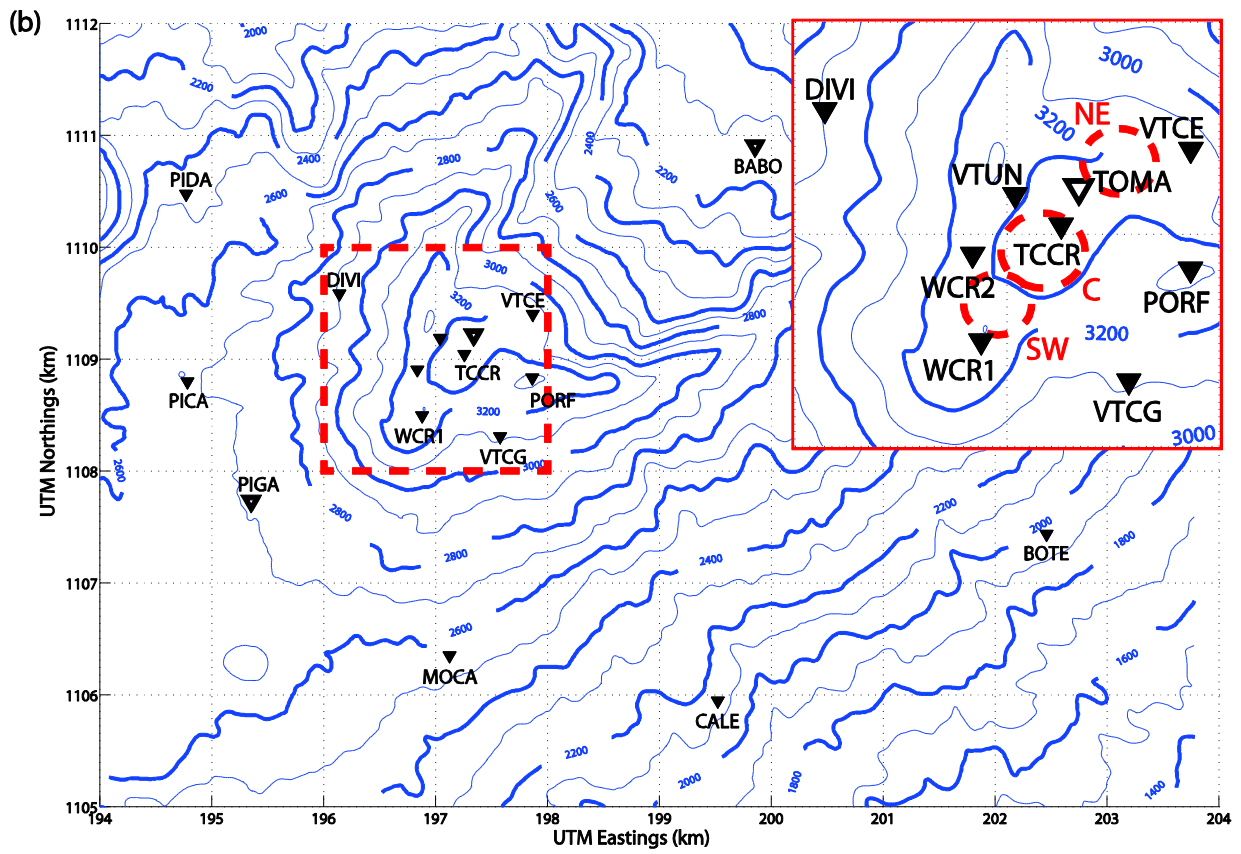
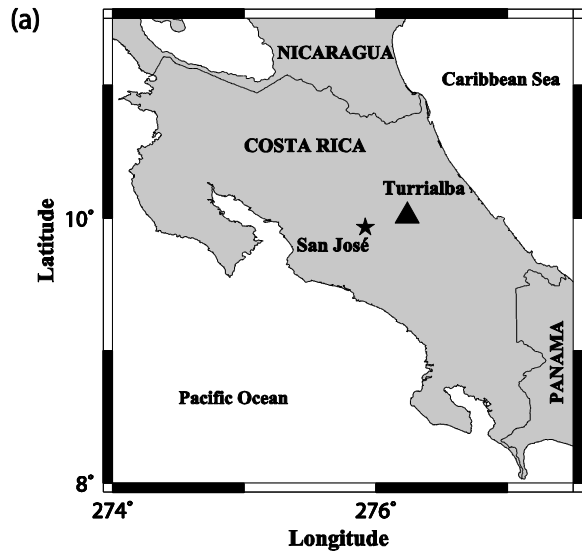
876 clustered, but there does appear to be a clear inverse relationship between corner frequency and
877 magnitude. A line of best fit (calculated using the L1 norm) is plotted through the data (red line),
878 with a slope of -2.04. A second line of best fit has also been calculated using the inverse of the
879 relationship, as the noise and the distribution of the event sizes can bias the linear regression and
880 is plotted as a dashed red line, with a gradient of -3.76. The theoretical -3 earthquake
881 relationship is also plotted (black with markers) and is also consistent with the data. (b) shows
882 examples of the fits between the smoothed spectra of 9 random LP events (blue), and the fitting
883 functions (red). The fits appear to be reasonable.

884

885

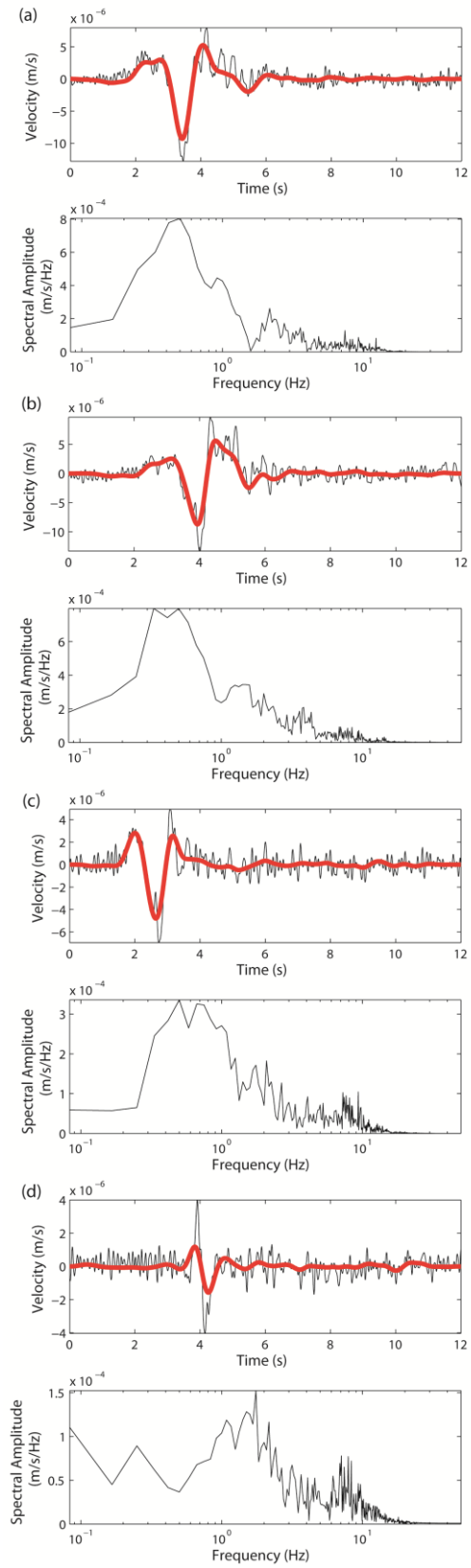
886

887



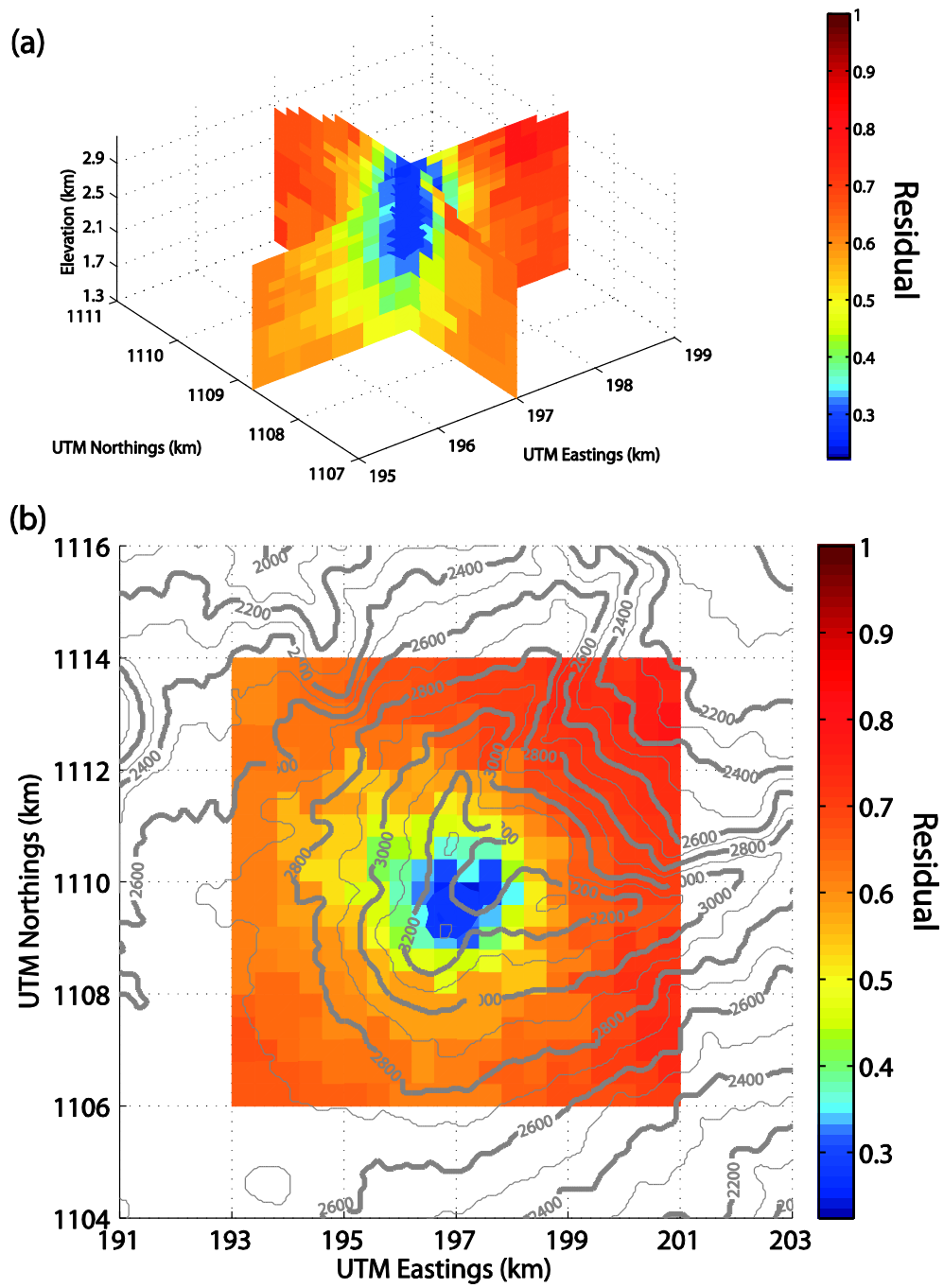
888

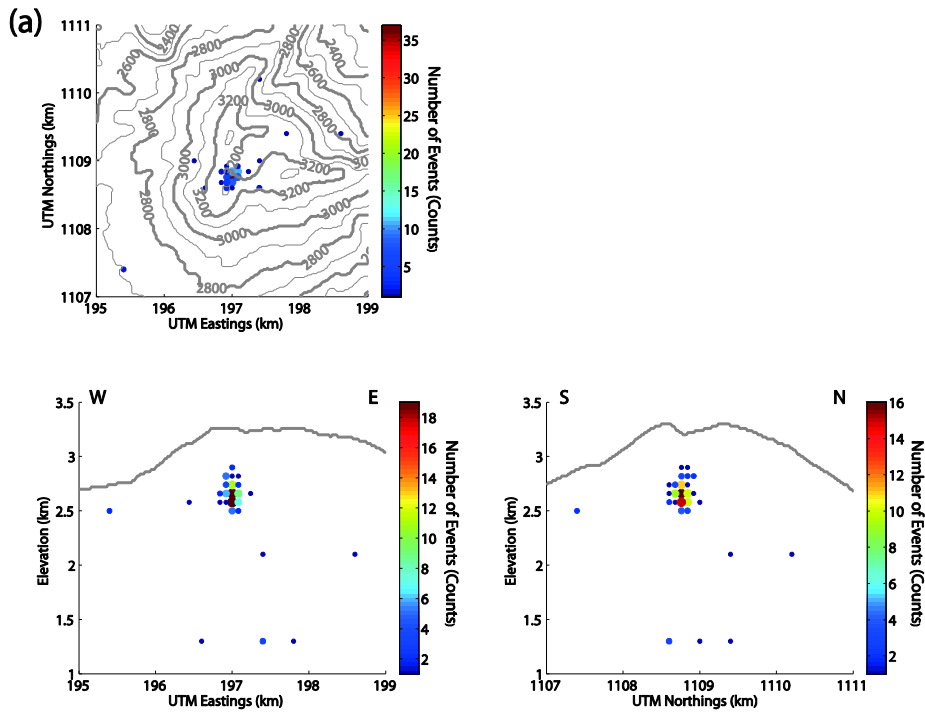
889 Figure 1



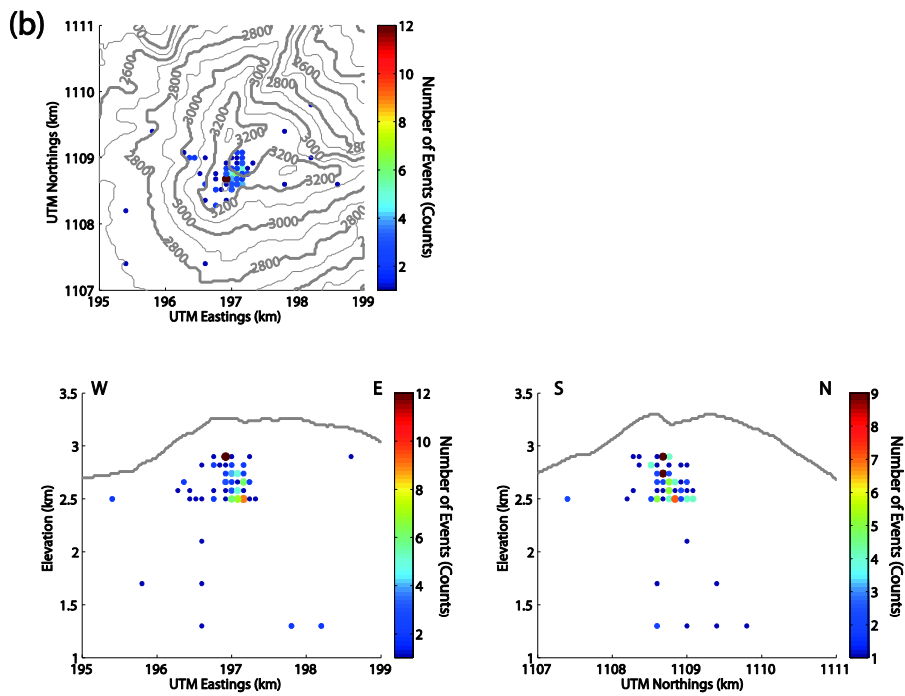
890

891 Figure 2





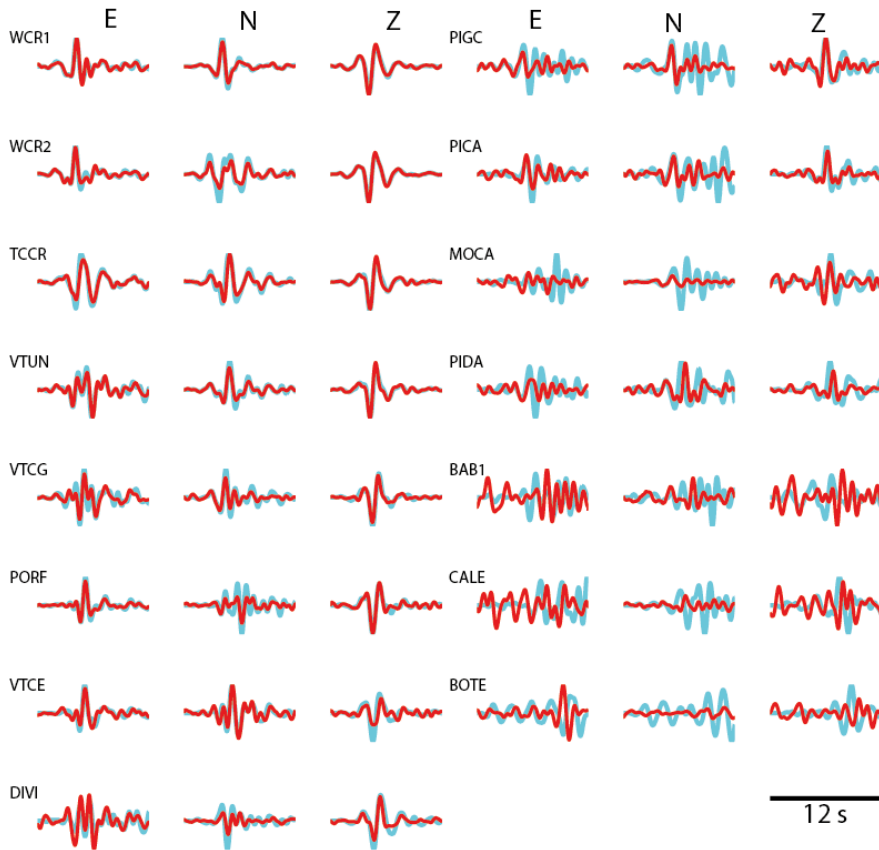
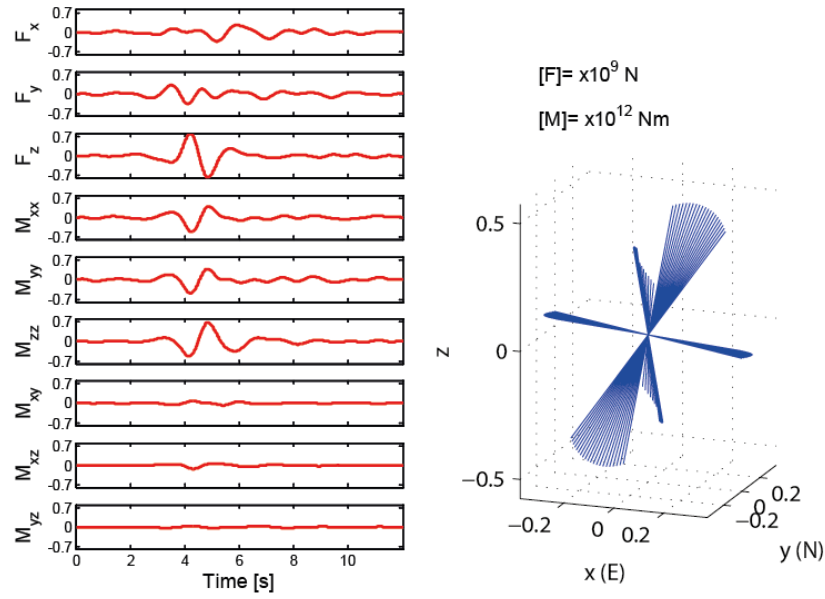
895



896

897 Figure 4

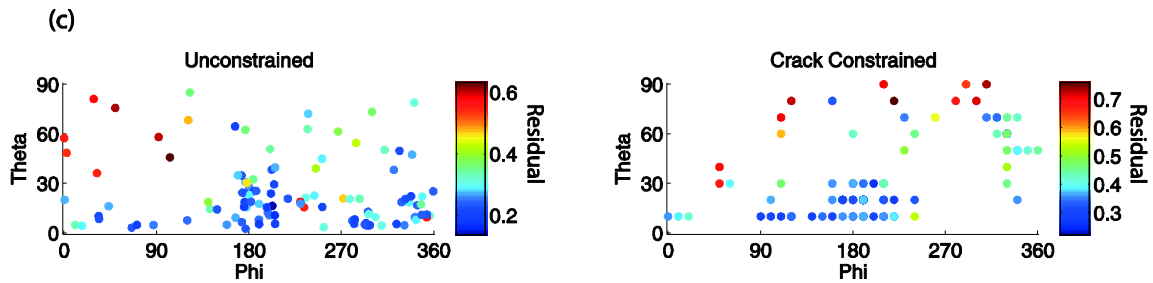
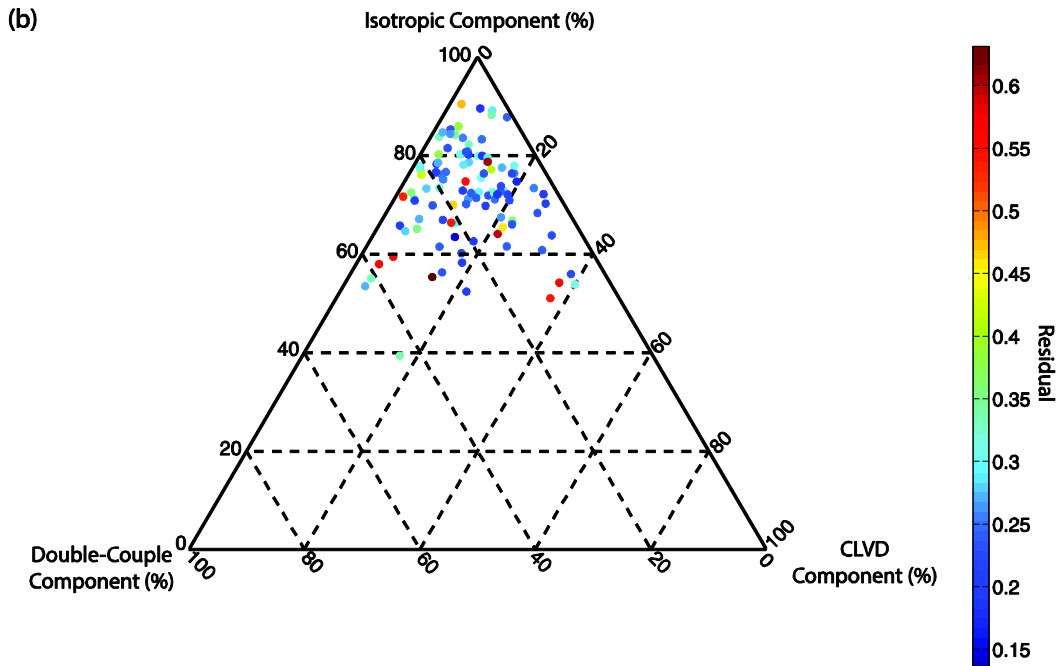
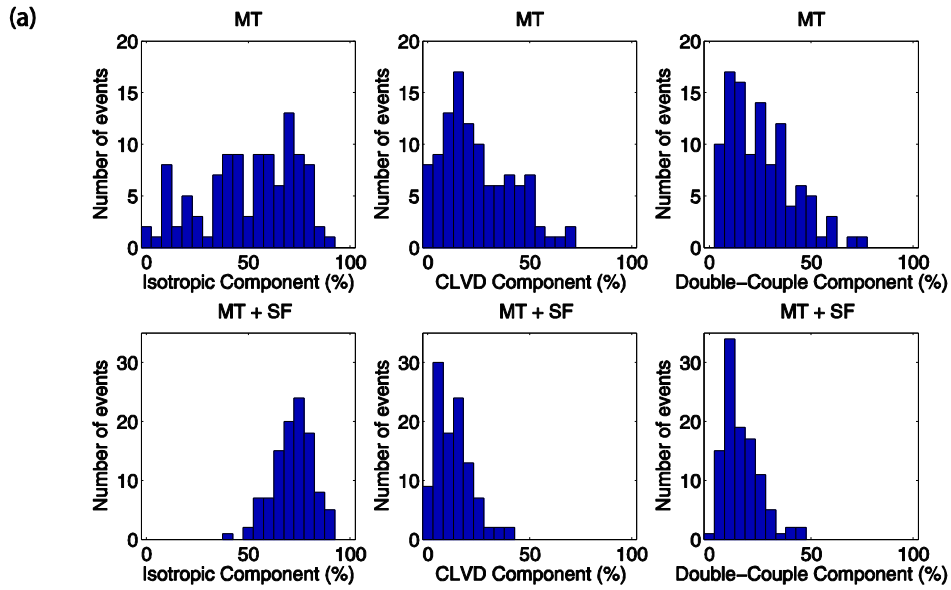
898



899

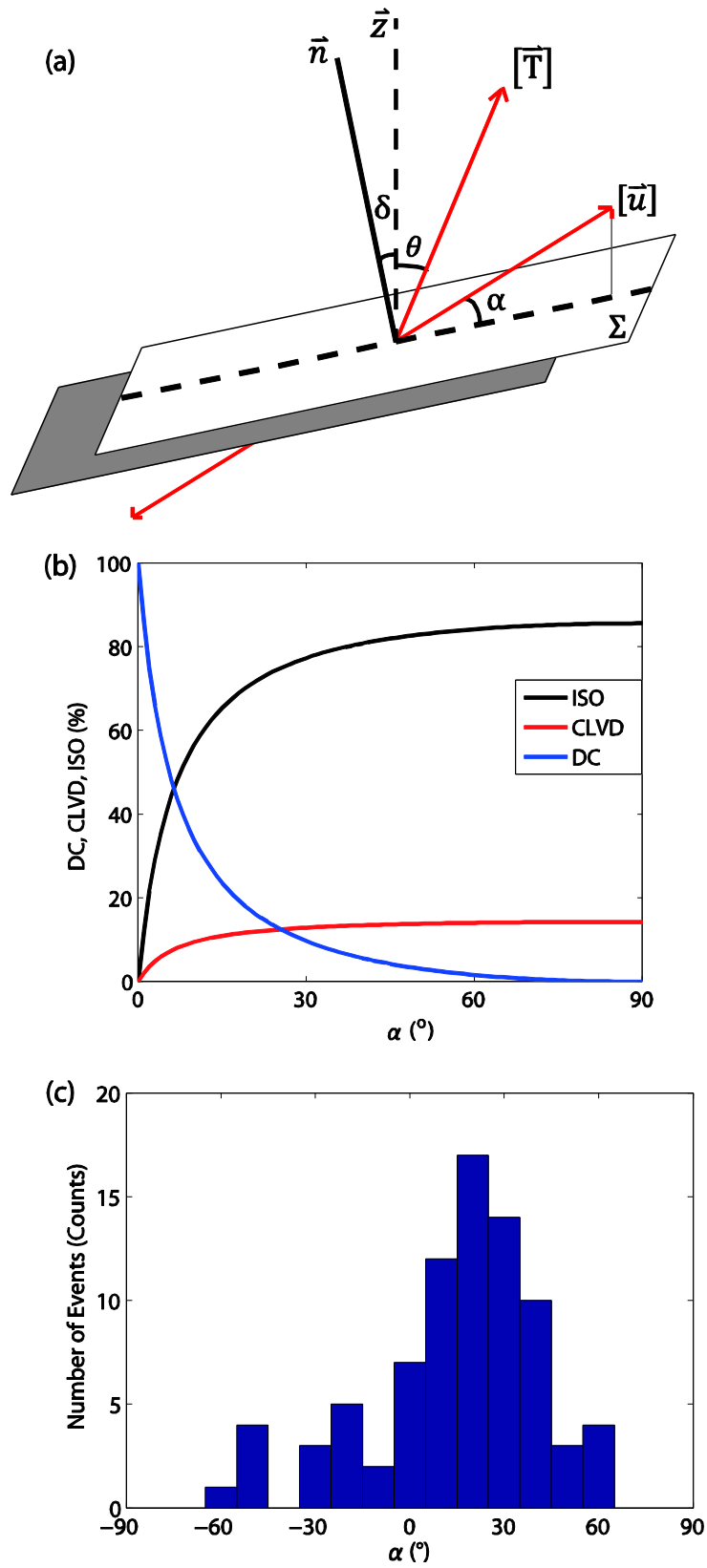
900 Figure 5

901



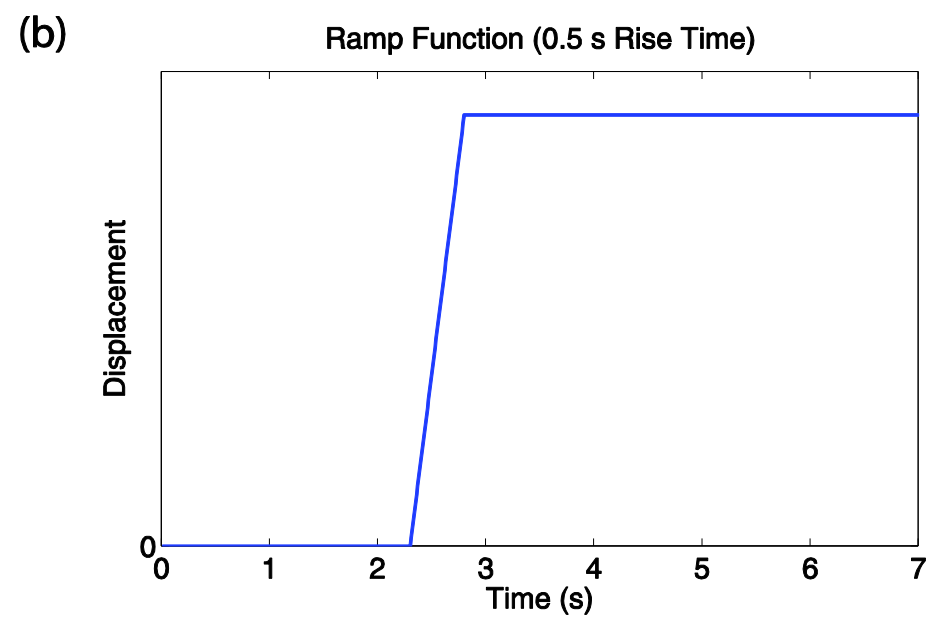
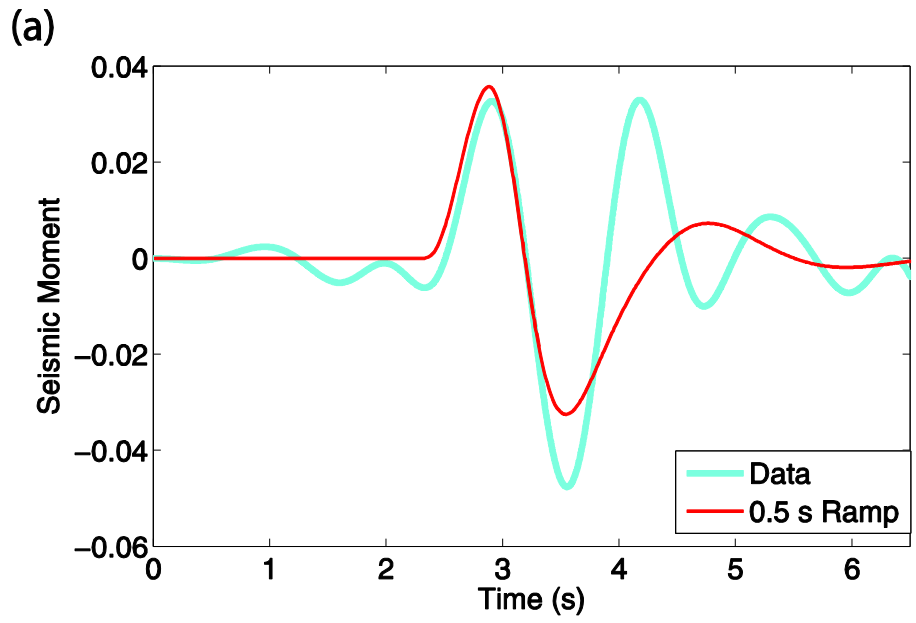
902

903 Figure 6



904

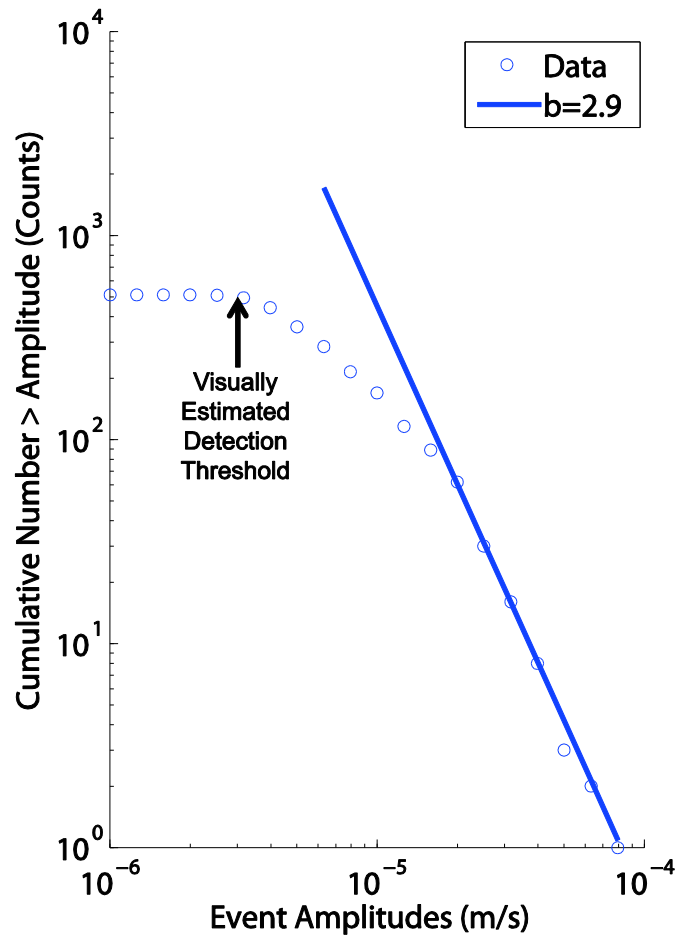
905 Figure 7



906

907

908 Figure 8

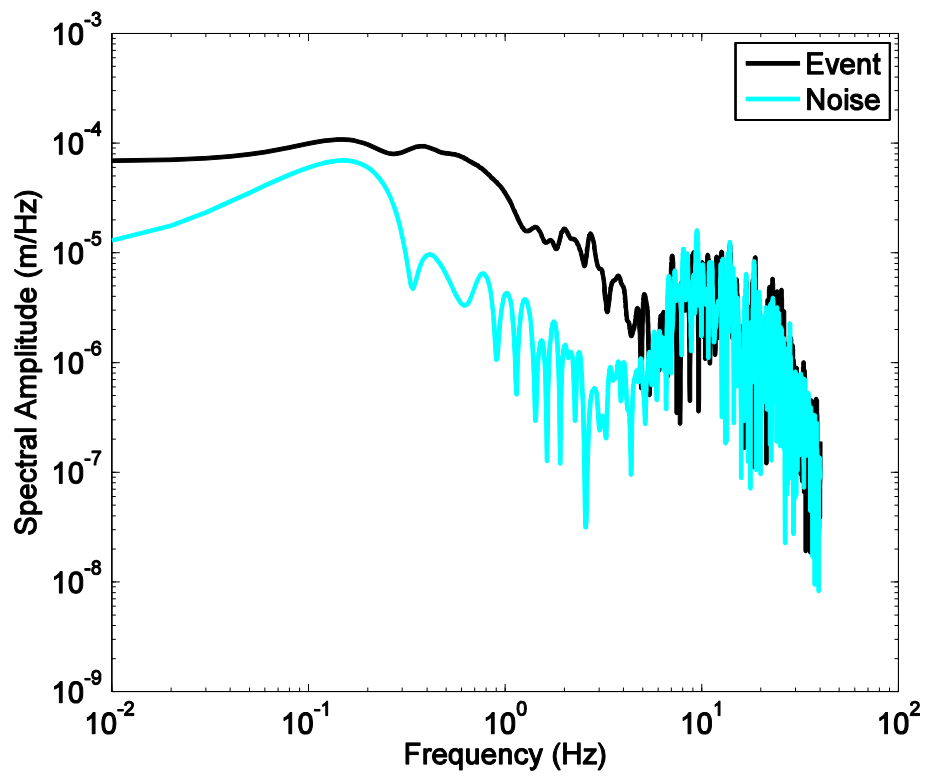


909

910 Figure 9

911

912

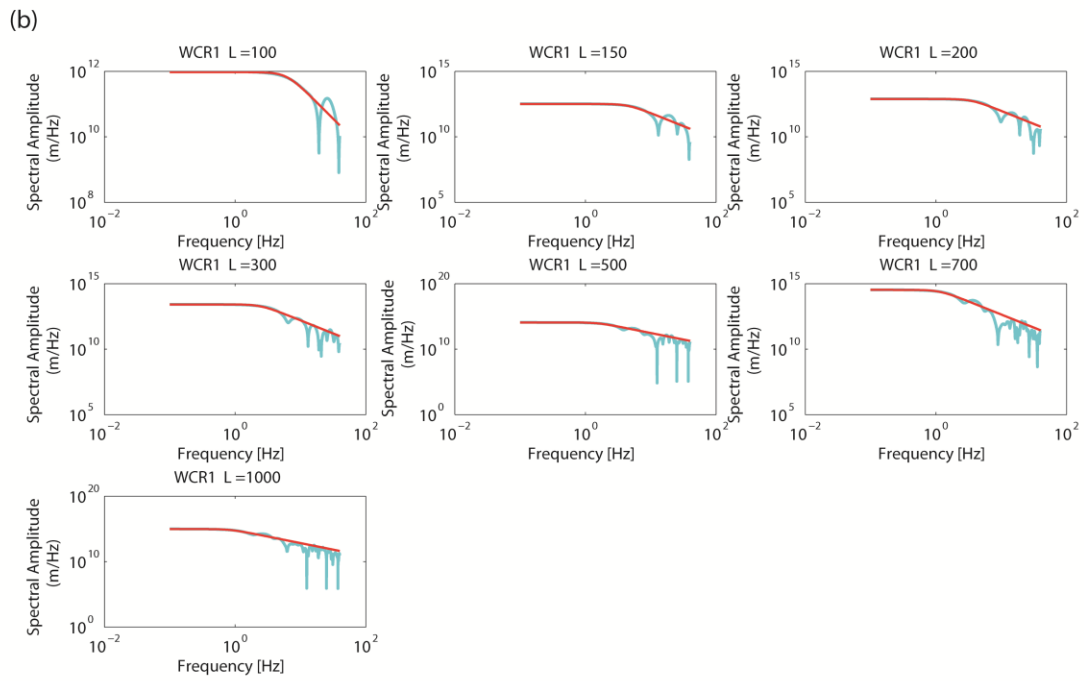
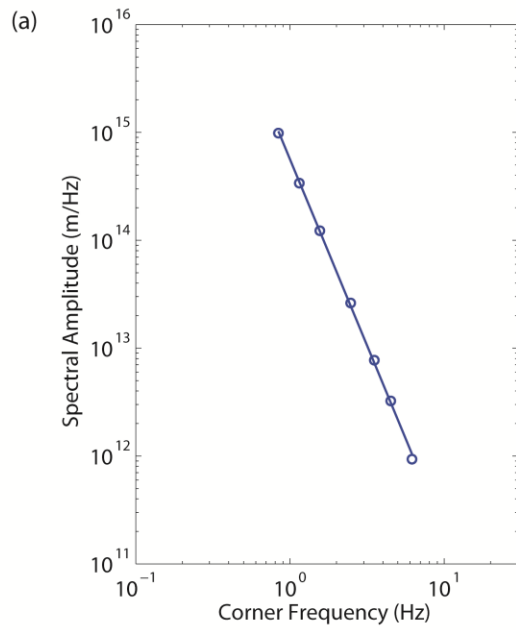


913

914 Figure 10

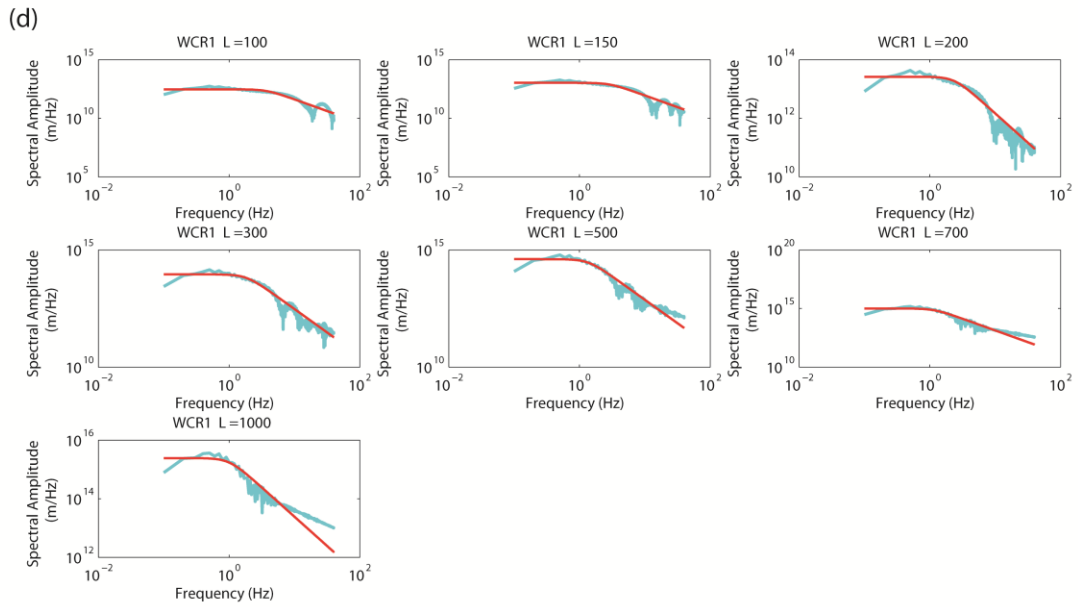
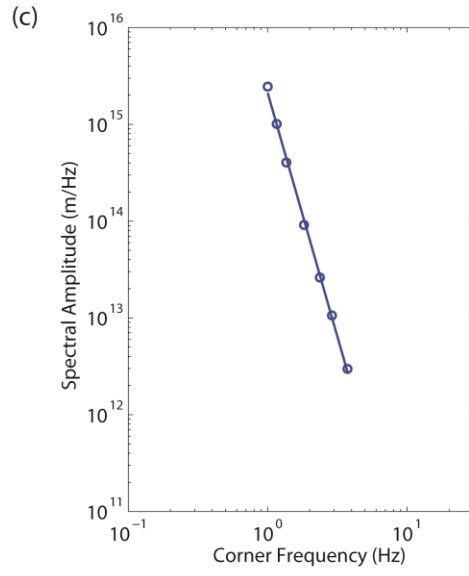
915

916



917

918

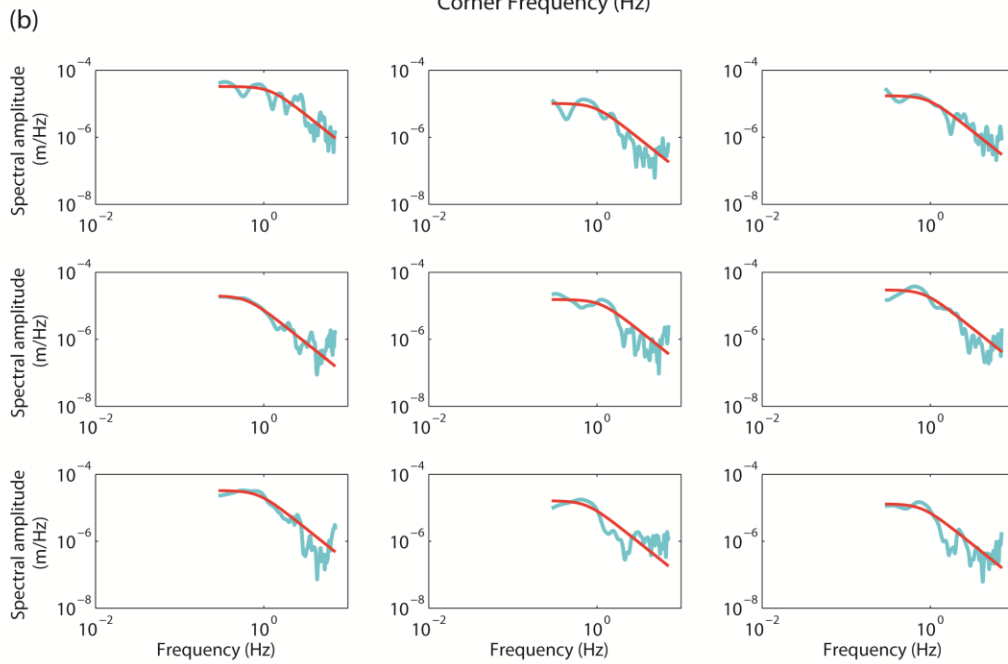
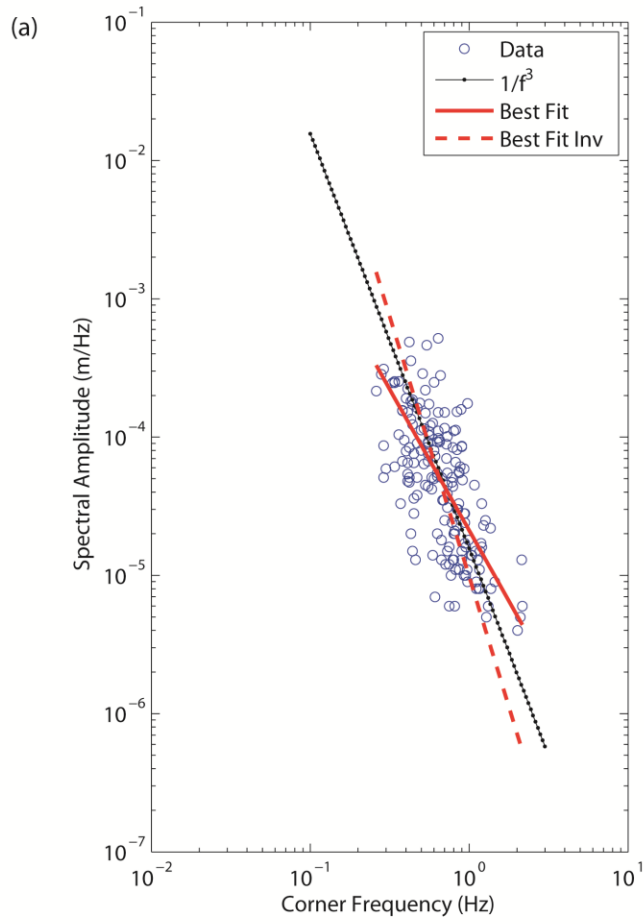


919

920 Figure 11

921

922



923

924 Figure 12